Journal of Materials Chemistry A

REVIEW

Cite this: J. Mater. Chem. A, 2016, 4, 5784

Achieving a high fill factor for organic solar cells

Meng-Huan Jao, Hsueh-Chung Liao and Wei-Fang Su*

Organic photovoltaics (OPVs) have developed rapidly in the last decades due to their potential for providing cost-efficient, low-energy consumption, and environmentally friendly renewable energy sources. Some research reports have focused on the device physics of organic photovoltaics that governs open circuit voltage (V_{oc}) and short circuit current (J_{sc}) to improve their performance. In this review, we focus on the third parameter, fill factor (FF), that is equally important in determining the power conversion efficiency. We discuss the mathematical calculation of the FF and the relationship between the FF and equivalent circuit model elements, namely, shunt resistance, series resistance, and diode ideal factor. In order to provide a strategy toward a high FF for OPVs from the viewpoints of device design and material synthesis, we review important device features and BHJ features that have a large impact on the device FF, including preventing shorting, buffer layer design, domain size or purity, gradated BHJ structures, π–π stacking distance or direction, *etc.* We hope this article can provide a comprehensive insight into elements controlling the FF of OPVs and give a valuable direction for better device and material design.

Received 6th January 2016
Accepted 9th March 2016

DOI: 10.1039/c6ta00126b

www.rsc.org/MaterialsA

1. Introduction

In recent years, organic photovoltaics (OPVs) have attracted intensive attention due to their advantages over traditional Si-based and inorganic thin film solar cells. These advantages include low temperature solution processability and mechanical flexibility[1–6] which enable OPVs to be manufactured by the cost-effective and energy-saving roll-to-roll process and to achieve the goal of grid parity.[6–13] Furthermore, light-weight, semitransparent and flexible OPV modules can be integrated into portable electronics, wearable gadgets, building windows and low power-consuming devices, *etc.*, opening new markets and applications for PV technology.[14]

All the special OPV features are derived from the materials used in device fabrication. To date, the most promising OPVs consist of either conjugated small molecules or polymers serving as donors and high electron affinity fullerene derivatives serving as acceptors. Both donor and acceptor contain mostly light elements such as C, N, O, H, and S, which are abundant and environmentally benign. Additionally, because of the tremendous advancement in the knowledge and synthesis of organic molecules, a myriad of chemical structures can be created. These new structures allow tunable optoelectronic properties resulting in great improvement in the performance of PVs, *e.g.*, the band gap, light-absorption coefficient, majority

Department of Materials Science and Engineering, National Taiwan University, Taipei 106-17, Taiwan. E-mail: suwf@ntu.edu.tw; Fax: +886-2-3366-4078; Tel: +886-2-3366-4078

Meng-Huan Jao received his BS and MS degree from the Department of Materials Science and Engineering at National Taiwan University in 2011 and 2013, respectively. Now he is a PhD student under the supervision of Professor Wei-Fang Su at the Department of Materials Science and Engineering, National Taiwan University. His research interests include device engineering and device physics in solution-processed optoelectronics.

Hsueh-Chung Liao received his Ph.D. in materials science and engineering from the National Taiwan University (2013) under the supervision of Professor Wei-Fang Su. Afterward, he joined Northwestern University as a postdoctoral researcher. His scientific interest includes the design, fabrication, and characterization of optoelectronics such as emerging photovoltaics and sensors.

carrier type, carrier concentration, and carrier mobility.[15–18] The possibility of many different materials makes the OPVs a fascinating technology in the PV field.

For this emerging technology of solar cells, one of the most obvious obstacles to commercialization is its relatively low power conversion efficiency (PCE). At present, the PCE has reached benchmark values over 10% for single junction devices[19–25] and over 11% for multiple junctions.[26–28] However, compared with their inorganic counterparts, there is still room for the improvement of PCE.

The PCE of solar cells is calculated according to eqn (1).

$$\mathrm{PCE} = \frac{V_{\mathrm{oc}} J_{\mathrm{sc}} \mathrm{FF}}{P_{\mathrm{in}}} \quad (1)$$

P_{in} is the incident power of sun. The numerator includes three important parameters of solar cells: open circuit voltage (V_{oc}), short circuit current density (J_{sc}), and fill factor (FF). The reason that the performance of OPVs is still lagging behind inorganic photovoltaic technologies can be attributed to the lower values of J_{sc} and FF. To improve J_{sc}, novel low band gap materials have been designed and synthesized. By morphology modulation and device structure optimization, devices with internal quantum efficiency (IQE) nearly 100% have been reported.[29] Nevertheless, the J_{sc} of the as-mentioned devices is still in the range of 10–15 mA cm^{-2}, which can be attributed to the particularly thin active layer of the devices. Many OPVs with outstanding FFs and performance consist of an active layer less than 100 nm.[30,31] It is possible to enhance the value of J_{sc} by adjusting the processing parameters to increase the film thickness. However, a concomitant drop of the FF is often observed, which leads to no improvement in PCE, or even worse, a lower PCE performance.[31] Besides, narrowing the band gap of the material is often accompanied by a negative impact on other performance factors. Therefore, it is not a suitable strategy to enhance the PCE. According to the consideration of spectrum loss in the calculation of the Shockley–Queisser limit, photons with energy less than the band gap will not contribute to the photocurrent and photons with energy greater than the band gap will lose the extra energy through heat dissipation. Therefore, it is obvious and detrimental that V_{oc} and J_{sc} must compromise with each other. Unrestrained increase of the band gap of the light absorption material to enhance the V_{oc} of the as-made device will ultimately lead to the decrease of J_{sc}, and *vice versa*. Therefore, the third parameter in eqn (1), FF, plays a critical role in further improvement of the PCE of OPVs.

In order to design better methods to improve the FF, one must first understand the mechanism behind the operation of OPVs. The mechanism of photon–electron conversion and the design of the device structure are slightly different for OPVs compared with conventional PV technology. According to the comprehensive charge generation mechanism of OPVs, the following stages are involved: (1) light absorption and exciton generation, (2) exciton diffusion, (3) exciton dissociation, (4) carrier transportation, and (5) carrier collection.[32–35] Typically, photon absorption in OPVs leads to the formation of a singlet state exciton, which is actually an electron–hole pair bound by coulombic force. Due to the generally low relative permittivity of organic materials (in the range of 2–4), the coulombic force between the electron and hole is so large that dissociation of this electron–hole pair by ambient thermal energy is nearly impossible. This electron–hole pair can be dissociated into the individual electron and hole only at the interface between the donor and acceptor where a locally intensive electric field exists. After successful dissociation, the electron and hole can be transported through the acceptor and donor domain, respectively, and finally be collected by electrodes.

The dissociation of the exciton is critical to the performance of OPVs. After generation, an exciton will make no contribution to the photocurrent if it relaxes back to the ground state or it is annihilated through geminate recombination in a short period.[36,37] To ensure effective generation of the photocurrent, the exciton must diffuse to the interface between the donor and acceptor before relaxation or recombination. The diffusion length of the exciton is in the order of 10 nm. As a consequence, the ideal nanostructure of OPVs is reckoned to be a bi-continuous interpenetration of the donor and acceptor domain with domain size at the scale of 10 nm. This three-dimensional donor–acceptor junction differs from the planar junction in traditional devices and is called the bulk-heterojunction (BHJ).

The mechanism described above influences the value of V_{oc}, J_{sc}, and FF. Fig. 1(a) shows the typical current density–voltage (*J*–*V*) characteristic curves under dark and illumination conditions. When the device is under illumination, V_{oc} is read from the voltage where no current passes through devices, and J_{sc} is read from the current density passing through devices when no external bias is applied. Under a particular applied bias with the corresponding current density, the power generated from this device will reach a maximum. This particular voltage and current density are called V_{max} and J_{max}, respectively. With the values given above, the FF can be calculated easily from eqn (2), which is the ratio of realistically achieved performance (V_{max}-J_{max}) over ideally achievable performance ($V_{\mathrm{oc}}J_{\mathrm{sc}}$). In other

Professor Su obtained her Ph.D. from the University of Massachusetts and did postdoctoral research in Northwestern University, USA. She joined Westinghouse Research Center to develop materials for electric/electronic applications for 16 years with 6 outstanding researcher awards. She is a distinguished professor in National Taiwan University. Her research is focused on the design, synthesis and processing of polymeric materials for electronic device/solar cell and medical applications. She was awarded 2011 Outstanding Researcher of Ministry of Science and Technology of Taiwan. She has published 186 SCI papers, 2 text books on solar cells (2012 Wiley) and polymers (2013 Springer) respectively, 27 US patents and 33 Taiwan patents.

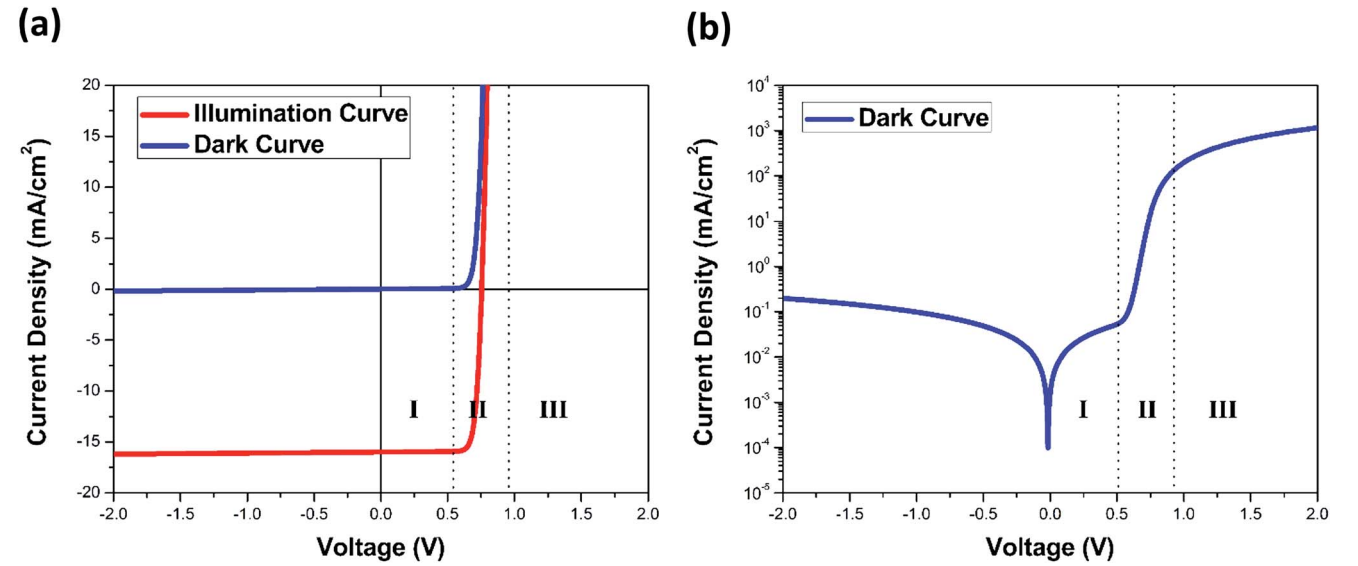

Fig. 1 (a) Typical current density–voltage (J–V) characteristic curves of a solar cell under dark (blue) and illumination (red) conditions by simulation. (b) Dark current of the solar cell depicted on log-linear scale using the absolute value of current density. From this figure, the curve can be divided into three regions according to the change of the slope. For regions I, II, and III, the behavior of the curve is dominated by the shunt resistance, diode ideality, and series resistance, respectively.

words, the FF stands for how the realistically achieved performance filled the ideally achievable performance.

$$\mathrm{FF} = \frac{V_{\max} J_{\max}}{V_{\mathrm{oc}} J_{\mathrm{sc}}} \tag{2}$$

The origins of V_{oc} and J_{sc} have been widely studied and an explicit theory and knowledge have been established.[38–41] However, the third parameter, FF, is more complex and less understood than the others. On the surface, the FF is a combined result from all the complicated interactions, such as the formation, diffusion, and dissociation of excitons; and the transportation and collection of carriers. In this review, we focus on the fundamental interpretation of the FF in terms of the device physics and find ways to improve the FF of OPVs.

2. Mathematical calculation of the fill factor

From the J–V plot and eqn (2), the FF can be understood as the degree of how rectangular, or the "rectangularity", a J–V characteristic curve exhibits. Alternatively the FF can be regarded as how easily photo-generated carriers could be swept out under the field resulting from the build-in potential and external applied bias. When photo-generated charge carriers can smoothly flow out of a device while the build-in potential is decreased by external applied bias, this device will present a high FF. For a photovoltaic device with the FF equal to 100%, the photo-generated current remains constant as long as the applied bias is smaller than V_{oc}. However, in reality, the FF can't reach 100%, not only for OPVs, but also for all the other photovoltaic technologies. This is attributed to the fact that photovoltaic devices are composed of p–n junction diodes, and thus the J–V characteristic curves behave more like exponential functions rather than step functions.[42,43]

Since the J–V characteristic curve can be considered as a function, then the calculation of the FF must be feasible if all the variables are given. A well-known study focusing on calculation and prediction of the solar cell FF derives a simple but accurate empirical expression:[44]

$$\mathrm{FF}_0 = \frac{v_{\mathrm{oc}} - \ln(v_{\mathrm{oc}} + 0.72)}{v_{\mathrm{oc}} + 1} \tag{3}$$

In this equation, v_{oc} stands for the normalized open circuit voltage, qV_{oc}/nkT, where n stands for the diode ideality factor, q is the elementary charge, and k is the Boltzmann constant. The accuracy of this expression approaches to one digit in the fourth significant place when the value of normalized open circuit voltages is larger than 10. This expression applies adequately to most of the photovoltaic technologies, including OPV. For example, the normalized open circuit voltage for P3HT:PCBM, which is one of the most representative systems in OPV, is about 24 when n is set as unity.

Nevertheless, in real applications, many non-ideal situations can lead to the loss of PCE and FF. One of them is the resistance in the device retarding or decelerating the current flow, which is denoted as series resistance, R_{s}. Another is the unwanted current leakage from the extra current path caused by small shunt resistance, R_{sh}. Now if R_{s} is taken into consideration, while shunt resistance R_{sh} is still large enough as in the ideal case, the expression for the FF can be modified into

$$\mathrm{FF}_{\mathrm{s}} = \mathrm{FF}_0(1 - r_{\mathrm{s}}) \tag{4}$$

where FF_0 is the result calculated from eqn (3), and r_{s} is the normalized series resistance $R_{\mathrm{s}}J_{\mathrm{sc}}/V_{\mathrm{oc}}$. The accuracy of this

expression can reach one digit in the second significant place, which is also good enough for application in most of the photovoltaic devices. On the other hand, if the shunt resistance R_{sh} is small and deviates far from ideality while the series resistance R_s is negligible, the expression for the FF can be modified into

$$FF_{sh} = FF_0\left[1 - \frac{(v_{oc} + 0.7)}{v_{oc}}\frac{FF_0}{r_{sh}}\right] \quad (5)$$

where FF_0 is calculated from eqn (3), v_{oc} is the normalized open circuit voltage, and r_{sh} is the normalized shunt resistance $R_{sh}J_{sc}/V_{oc}$. The accuracy of one digit in the third significant place can be accomplished by this expression, which is again good enough to be applied in most of the photovoltaic technologies including OPV. Finally, if both parasitic resistances are deviated from ideality and have to be taken into account, which is often the real case for OPVs, a simplified and approximated expression for the FF is shown as follows:

$$FF_{s+sh} = FF_s\left[1 - \frac{(v_{oc} + 0.7)}{v_{oc}}\frac{FF_s}{r_{sh}}\right] \quad (6)$$

where FF_s is calculated from eqn (4). Using this expression, accuracy with one digit in the second significant place can be reached.

The idea of series resistance, shunt resistance, and ideality factor can be explained more clearly by the equivalent circuit model. An ideal p–n junction photovoltaic can be depicted as the equivalent circuit shown in Fig. 2(a).[45–47] J_{ph} stands for the photo-generated current density, which is only dependent on the illumination light intensity, simulated here as a constant current source. J_d stands for the diode current density, which can be manipulated by the external applied voltage, V. The total current density, J, is the combination of J_{ph} and J_d, as given by eqn (7), where J_s is the diode saturation current density, q is the elementary charge, and k is the Boltzmann constant.

$$J = J_d - J_{ph} = J_s\left[\exp\left(\frac{qV}{kT}\right) - 1\right] - J_{ph} \quad (7)$$

In the real case, the J–V characteristic curve of the photovoltaic device deviates from the ideal one for a number of reasons. For instance, some defects such as pin holes and traps can substantially contribute as recombination sites and cause unwanted current leakage. In addition, series resistance can be introduced when carriers travel from the interface of the p–n junction to the buffer layer and finally to the electrode. Therefore, in order to have a more comprehensive perspective of how real photovoltaic device works, a modified equivalent circuit is presented, as shown in Fig. 2(b). In this modified simulation, the diode and constant current source are unchanged, while the ideality of the diode can be tuned by the parameter n, and the parasitic resistances, R_s and R_{sh}, are introduced, which are connected with the circuit in series and parallel, respectively. The series resistance R_s stands for a non-ideal voltage drop in the circuit while R_{sh} stands for current leakage in the real device. Based on the modified equivalent circuit, a new relationship between J–V can be derived as eqn (8).

$$J = J_s\left[\exp\left(\frac{q(V - JR_s)}{nkT}\right) - 1\right] + \frac{V - JR_s}{R_{sh}} - J_{ph} \quad (8)$$

This equation derived from the modified equivalent circuit works quite well on traditional inorganic photovoltaics. Although there are some differences between inorganic and organic solar cells in terms of material properties, the photon–electron conversion mechanism, and the device structure, eqn (8) can be applied to OPVs well.[34,48] As indicated in eqn (8), the output power of the device, which is the product of current density J flowing through the device and the applied bias V, can be expressed as a function of applied bias V. The specific bias V_{max} gives this function a maximum value, which is the so-called maximum output power point. By evaluating the specific V_{max}, the FF and PCE can be obtained.

All of the above expressions provide ways to calculate and evaluate the FF of a given device when all its equivalent circuit variables are given. Although those expressions are derived with some empirical approximation, they give good accuracy and are ready to be applied in most of the photovoltaic technologies including OPV. In other words, a tool for finding the FF by using variables introduced from the equivalent circuit model is established. From here, we raise the question: how do those variables affect the behavior of the FF? Or more accurately, how do those variables affect the shape of the J–V characteristic curve? In the following section, our discussion will focus on the critical examination of the J–V characteristic curve and on how it impacts the inter-corresponding relationship between R_s, R_{sh}, n and FF.

As shown in the schematic diagram of Fig. 1(a), there are two curves in the J–V plot. The curve passing through the origin is usually called as the "dark curve", which is obtained by measuring the device under dark conditions. The other curve passing through the fourth quadrant is called the "illumination curve", which is obtained by measuring the device under illumination conditions. The PCE is calculated from the illumination curve. A good illumination curve can be taken as a vertical displacement in the J–V plot (the amount of displacement is equal to the J_{sc}) of its counterpart dark curve, possessing a shape close to a rectangle in the fourth quadrant and thus representing a high FF and PCE.

Interestingly, when the J–V plot is re-plotted with a semi-log scale instead of a linear scale, as shown in Fig. 1(b), the J–V curve can be divided into three regions with different slopes. In region I where applied external bias changes from negative to

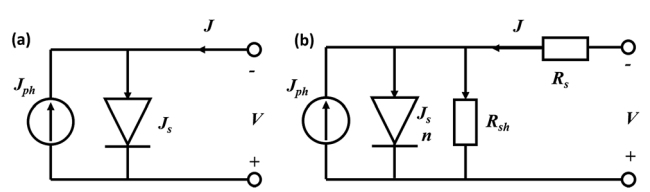

Fig. 2 (a) Ideal equivalent circuit model of a solar cell. J_s stands for the diode saturation current density. J_{ph} stands for the photocurrent density. (b) Practical equivalent circuit model considering the shunt resistance (R_{sh}), diode ideality (n), and series resistance (R_s).

low positive voltage, the *J–V* curve performs close to a straight line with a slope of R_{sh}^{-1} approximately. It is beneficial to avoid the conditions leading to a decreased R_{sh} in order to obtain a high FF value. In most photovoltaic devices, it means to prevent current leakage through pin holes and traps or current leakage from the edge of cells. In OPVs, due to their distinctive BHJ structure that both donor and acceptor materials have contacts with the same carrier collection electrode, one additional pathway for current leakage comes from the bimolecular recombination near the interface between the active layer and electrode. This extra pathway for current leakage must be reduced or eliminated in the OPV device.

In region II, the shape of the *J–V* characteristic curve makes an abrupt turn and the slope changes quite a lot due to the dominance of the exponential term when the external bias switches from low voltage to nearly open circuit voltage. In this region, *n*, the ideality factor, controls the "rectangularity" of the *J–V* characteristic curve. In fact, the overall behavior, *i.e.* the shape of the *J–V* characteristic curve, can largely depend on the value of *n*. Ideally, the value of the ideality factor is equal to unity, which is usually the case for Si based solar cells because of the dominance of the diffusion current and little recombination arises in the space charge region. In OPVs, however, due to their distinctive BHJ structure and their intrinsic large exciton binding energy (about 0.3–0.5 eV),[33,49] the recombination effect cannot be neglected and *n* deviates from unity.[42] Researchers classify the OPV recombination effects into two kinds: the geminate recombination which stands for recombination before the exciton has a chance to split into free charges, and bimolecular recombination which stands for recombination occurring after the exciton is split into the individual electron and hole.[50]

In region III, where applied external bias is larger than V_{oc}, the *J–V* response again behaves like a straight line with a slope about R_s^{-1}. Apparently, to have a high FF, the R_s is expected to be as small as possible. In a practical device, R_s mostly comes from the bulk resistance of the active layer or from the contact resistance between the active layer and electrode. Incompatible band alignment can lead to a large R_s value and s-shaped *J–V* curve, causing a dramatic decrease in the FF and PCE.[51,52] In OPV systems, a transparent conducting electrode of ITO is widely chosen as the device electrode. The conductivity of ITO is good enough for laboratory scale devices. However, it may not be adequate for large scale devices.[53] Therefore, when fabricating large scale OPV devices, the R_s caused by the limited conductivity of ITO must be taken into consideration.

In the above section, the shape of the *J–V* characteristic curve and the accompanying change of the FF are discussed in terms of the equivalent circuit model. A good FF can be theoretically achieved by minimizing R_s, maximizing R_{sh}, and reducing *n* to unity. There is a detailed article discussing the FF of OPVs from the viewpoint of the equivalent circuit model.[54] These can greatly help experimentalists to diagnose their devices by *J–V* characteristic curves and to point out the deficiency that still has room for improvement. However, these concepts lead to only limited improvement.

Unlike inorganic solar cells, most OPVs have BHJ structures, resulting in special characteristics which do not exist in inorganic solar cells but have a great influence on the FF of OPV devices. These special characteristics include domain size, vertical gradient, packing distance of molecules, packing orientation, and domain purity. In the following sections, we first discuss some methodologies related to device features to reduce R_s and increase R_{sh}, which can eventually lead to a high FF. Then we focus on the BHJ features that can impact the device FF and how to tailor these features to a high FF.

3. Effects of device features on the fill factor of OPVs

3.1. Shorting

Shorting in any photovoltaics will lead to unwanted current leakage and detrimental loss of the FF and efficiency. Therefore, elimination of shorting is the basic principle when designing and fabricating devices. In OPV technology, generally the film thickness of the photoactive layer is in the range of 100–300 nm.[55] As a consequence, the unwanted current leakage may arise from inter-electrode shorting when the roughness of the substrate is in the order of a few hundred nm. The shorting-induced current leakage is a frequent and troublesome issue when applying silver nanowires (Ag NWs) as the transparent electrode in OPVs.

Coating Ag NWs usually results in rough topography with peak height greater than 100 nm due to inevitable overlapping of Ag NWs,[56–63] which has a diameter of about tens of nanometers. It is a difficult task to decrease the roughness by using a simple coating technique. Thus, the as-prepared OPV devices with the thickness of the active layer less than 300 nm often suffer from detrimental current leakage due to inter-electrode shorting. A R_{sh} of less than 0.1 kΩ cm^2 has been reported to lead to a poor FF. Fig. 3 shows the results of a series of experiments aiming to resolve this problem.[64] In their experiments, researchers aim to fill the voids between Ag NWs by using conducting polymer PEDOT:PSS. When a PEDOT:PSS film of about 30 nm thickness is deposited on top of Ag NWs electrode, the roughness decreases. However it is still not smooth enough for an OPV device. The upper plot of Fig. 3 shows that the as-prepared device (Ag NWs/PEDOT (30 nm)) has large dark current density on the order of 10 mA cm^{-2} during reverse bias,

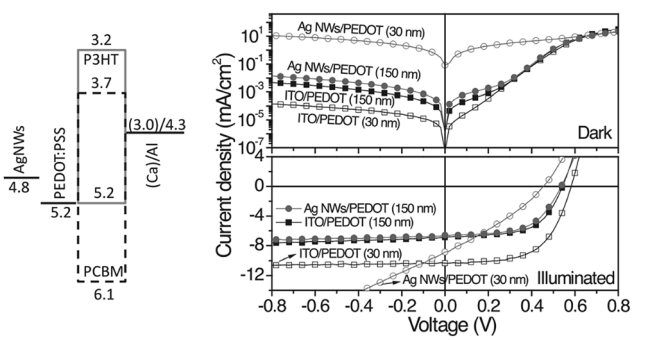

Fig. 3 Illustration of the energy level diagrams for Ag NWs/PEDOT/P3HT:PCBM/Ca/Al devices and the corresponding *J–V* characteristic curves. Reproduced with permission from ref. 64. © Wiley.

compared to the case for ITO of about 10^{-4} mA cm^{-2}. As a consequence, the device based on Ag NWs/PEDOT (30 nm) as the bottom electrode exhibits a *J–V* characteristic curve with a poor FF and R_{sh} less than 0.1 kΩ cm^2 under illumination. When the researchers increase the film thickness of PEDOT:PSS to about 150 nm covering the Ag NW electrode, the rough surface is nearly flattened and the current leakage is reduced, corresponding to a small dark current under reverse bias. Under illumination, the *J–V* characteristic curve of this device shows an improving trend with better shunt resistance (greater than 700-fold increase) and higher FF.

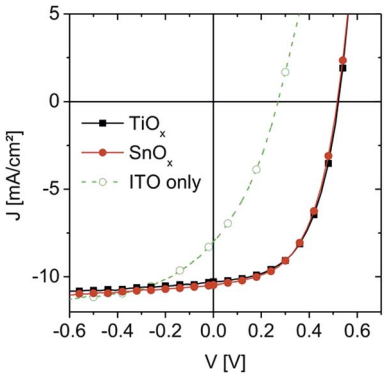

Fig. 4 The *J–V* characteristic curves of three devices with different electron transport layers, namely, TiO_x, SnO_x, and bare ITO. Reproduced with permission from ref. 65. © Royal Society.

3.2. Buffer layer

In the OPV technology, buffer layers play a unique and irreplaceable role. Without buffer layer, OPVs can only achieve moderate efficiency due to the significant occurrence of recombination. Sometimes a good buffer layer not only suppresses troublesome recombination but also induces a donor–acceptor distribution gradient that facilitates selective carrier transport. The reason for the multi-functional contributions by the buffer layers is the distinctive photo–electron conversion mechanism and device architecture.

After photo-generated excitons dissociate into electrons and holes, those carriers are transported by the corresponding acceptor and donor materials to the electrodes. Ideally, electrons are expected to be transported to the cathode, and holes to the anode. However, due to the distinctive BHJ structures of most state-of-art OPV devices, both acceptor and donor materials have contacts with both electrodes. These contacts allow both kinds of carriers to be transported to both electrodes, causing undesirable recombination near electrodes.

Fig. 4 shows three *J–V* characteristic curves of inverted OPV devices.[65] The device employing only ITO as the cathode exhibits a poor FF and PCE due to the strong recombination near the ITO cathode. Under the condition of zero external bias, an internal electric field from the cathode to anode exists, causing electrons and holes to drift toward the cathode and anode, respectively. However, this internal field is not strong enough to sweep all the holes into the anode. There are still chances for holes to reach the cathode by travelling through the donor material path, and *vice versa*. When an external bias is applied in the direction opposite to the internal field, which is the case when characterizing the fourth quadrant of the *J–V* response, the internal field is gradually cancelled and its ability to drift carriers to the desired electrode further decreases, causing significant recombination near the cathode, in this case, ITO. Thus, a dramatic decrease in current density with increasing external bias, as observed in Fig. 4, causes an adverse effect on the FF.

It is worth noting that, unlike the case of current leakage through inter-electrode shorting where a monotonic increase of current density is observed, a nearly constant current density can be reached when the external bias is in the same direction as the internal field, as comparing the third quadrant of Fig. 3 and 4. This is reasonable because nearly all the electrons and holes can be swept to the desired electrodes as the external and internal fields are aligned together. As a result, the current density saturates and remains constant with even "higher" external bias.

To solve this recombination issue, holes travelling and injecting into the cathode must be prevented. A buffer material inserted between the BHJ and cathode can serve as a hole blocking layer. Materials useful as hole blocking layers usually have a deep valence band maximum or highest unoccupied molecular orbital, HOMO, to suppress injection of holes into the cathode. Fig. 4 shows the effect of the hole blocking layer. In that experiment, TiO_x or SnO_x, which has a valence band maximum of about 7.7 eV, is used as the hole blocking layer and inserted between the BHJ and ITO. The *J–V* characteristic curves of the devices with TiO_x or SnO_x as the hole blocking layer show a nearly constant current density under negative and low positive applied bias, indicating little recombination at the cathode, leading to a better FF compared to the device with only ITO as the cathode. In this section, we discuss only the recombination at the cathode and hole blocking layer for clarity purposes. Of course, it is equally important to insert an electron blocking layer between the anode and BHJ to facilitate the transportation of holes.[66–69]

In addition to being a blocking layer, the buffer layer plays another role in determining the FF of OPVs. In the earlier part of this article, we mentioned that smaller series resistant, R_s, leads to a higher FF. The R_s is mostly determined by the contact resistance which arises from the interface between the electrode and active layer in OPV. This interface-induced contact resistance has a dominant effect on the OPV performance. To reduce the contact resistance, constructing a barrier-less interface for carrier extraction is a straight-forward solution. In other words, forming an ohmic contact between the electrode and active layer can minimize the contact resistance and increase the FF of the device.[70–73]

This can be done by choosing an electrode with appropriate work function relative to the active layer. Alternatively, it is more efficiently accomplished by inserting a buffer layer with adequate energy level alignment. Thus, as discussed earlier, the buffer layer in OPVs plays two imperative roles, one is to increase carrier selectivity and increase R_{sh}, the other is to form

a barrier-less ohmic contact and decrease R_s. As a consequence, a good selection of the buffer layer on both sides of an active layer can ultimately increase the FF and PCE.[74–76] The detailed working mechanism and comprehensive material development of the buffer layer have been reviewed previously.[77–79] In the following section, we will briefly describe the importance of matching work function and examples of some OPVs that achieve a high FF by the exquisite selection and design of the buffer layers.

Fig. 5(a) shows the *J–V* characteristic curves from a device with layered structure: ITO/C_{60}/CuPc/MoO_3/Ag.[80] This device structure indicates that the MoO_3 modified Ag electrode serves as the hole collection anode, ITO as the electron collection cathode, CuPc as the donor material, and C_{60} as the acceptor material. At the Ag anode side, designers insert a thin layer of MoO_3 with a deep conduction band[81,82] to form an ohmic contact with CuPc. Unlike the Ag anode side, a bare ITO is employed as the cathode to collect electrons. ITO has a work function of 4.7 eV and is in the middle of the band gap of C_{60} (the energy level of the HOMO and LUMO is 6.2 and 4.1 eV, respectively). In this scenario, a Schottky contact is formed between ITO and C_{60} with an energy barrier height approximately equal to the work function difference of ITO and the lowest unoccupied molecular orbital (LUMO) of C_{60}, as dictated by the Schottky–Mott model.[83,84] As a result, this energy barrier leads to a voltage drop at the contact and deteriorates the FF of the *J–V* characteristic curve and the device PCE.

Interestingly, it is reported that with continuous UV light illumination or under AM 1.5 conditions (containing UV light), the work function of ITO is prone to decline from 4.7 to about 4.2 eV,[85] approaching 4.1 eV for the LUMO of C_{60}. In other words, the contact between ITO and C_{60} can be gradually changed from Schottky type to ohmic type under prolonged illumination of UV light. This phenomenon is clearly demonstrated by the *J–V* characteristic curves in Fig. 5(a). At 0 min illumination time, the adverse work function mismatch leads to a great energy barrier and contact resistance, indicated by the slope of the *J–V* characteristic curve near V_{oc} and thus results in a poor FF and PCE. As the illumination time increases, the mismatch of work function and the contact resistance decrease. The slope near V_{oc} changes drastically. All these changes lead to a significant increase of FF and PCE. However, the movement of ITO work function is only a temporary modification rather than a permanent change. Hence it always takes a period of time to reach the best performance of such a device when illuminated.

Fortunately, this troublesome contact resistance issue can be solved by inserting an adequate buffer layer to modify the work function of ITO and to achieve a high FF at the very beginning of light illumination, as shown in Fig. 5(b). This device is constructed by the layer structure of ITO/PEIE/C_{60}/CuPc/MoO_3/Ag, which consists of the same device structure as in Fig. 5(a), except for coating a thin layer of PEIE on ITO before the deposition of C_{60}. The PEIE can modify the work function of ITO to be about 4 eV.[86,87] In this case, an ohmic contact is formed due to the close energy level alignment between PEIE-modified ITO and C_{60} regardless of the illumination time. The small R_s attributed to the low contact resistance leads to an improved FF and PCE.

Liao and co-workers[76] presented another example of highly efficient OPVs with a FF of 74% using a dual doped metal oxide as an electron transport layer in the inverted type device. By adding both an indium salt and a fullerene derivative into a ZnO precursor solution, they attained a dual doped In–ZnO–BisC_{60} thin film, with the concentrated fullerene derivative at the surface (interface between the electron transport layer and active layer) and concentrated indium at the bottom (interface between the electron transport layer and ITO cathode). This architecture enhances the conductivity and electron mobility of ZnO. Furthermore, the fullerene-rich surface may impede the donor materials from attachment to the electron transport layer and reduce the chance of surface recombination. The overall strategy makes this novel electron transport layer a promising material by simultaneously minimizing R_s and maximizing R_{sh}. Compared with pristine ZnO, the OPV device using In–ZnO–C_{60} as the electron transport layer exhibits an over 10% increase of FF.

In the inverted type OPVs, the electron transport layer is located between the active layer and transparent electrode. Hence, the optical transparency is a critical criterion. On the other hand, the light transmittance is not a required property

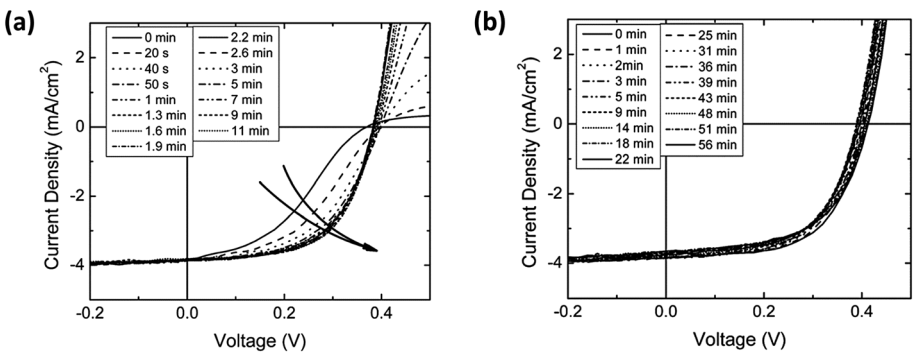

Fig. 5 (a) The *J–V* characteristic curves showing the device performance influenced by the work function change of ITO during AM 1.5 illumination. (b) The *J–V* characteristic curves of the device with PEIE modified ITO as the cathode. Reproduced with permission from ref. 80. © Royal Society.

Table 1 Examples of high FF OPVs utilizing novel buffer layers

ETL[a]	HTL[a]	Device structure	FF (%)	PCE (%)	Ref.
ETL-1	PEDOT	ITO/HTL/DR3TSBDT:$PC_{71}BM$ (M2)/ETL/Al	73	9.9	88
ZrAcac	PEDOT	ITO/HTL/PDBT-T1 (P8):$PC_{71}BM$/ETL/Al	75	9.7	89
$PrC_{60}MA$	PEDOT	ITO/HTL/DR3TBDTT:$PC_{71}BM$ (M3)/ETL/Al	76	9.5	90
PFNSO	PEDOT	ITO/HTL/PTB7:$PC_{71}BM$/ETL/Al	73	8.7	91
Ba	PEDOT	ITO/HTL/*p*-DTS$(FBTTh_2)_2$:$PC_{71}BM$/ETL/Al	74	8.6	74
PFCn6:K^+/Ca	PEDOT	ITO/HTL/P3HT:ICBA/ETL/Al	72	7.5	92
Ca	ReO_x	ITO/HTL/P3HT:ICBA/ETL/Al	77	7.2	93
PFN	MoO_3	ITO/ETL/PTB7-Th:$PC_{71}BM$/HTL/Al	73	10.6	22
In–ZnO–$BisC_{60}$	MoO_3	ITO/ETL/PTB7-Th:$PC_{71}BM$/HTL/Ag	74	10.3	76
ZnO/PFN-OX	MoO_3	ITO/ETL/PTB7:$PC_{71}BM$/HTL/Al	74	9.2	94
ZnO/C-PCBSD	PEDOT	ITO/ETL/P3HT:ICBA/HTL/Ag	72	7.3	75

[a] ETL and HTL stand for the electron transport layer and hole transport layer, respectively.

for the conventional type OPVs when an electron transport layer is located between the active layer and back electrode. Low work function metal with strong electron affinity, such as Ca, is one of the best candidates to serve as the electron transport layer in conventional OPVs (yet caution should be taken to address the stability issue due to the ease of oxidation of low work function metals). In the work by Gupta *et al.*,[74] they used Ba as an electron transport layer in conventional type OPVs and demonstrated high performance OPVs with a FF of 75%. They found that inserting a thin layer of Ba between the active layer and back electrode can greatly reduce the Shockley–Read–Hall recombination process, due to the successful passivation of surface traps. Additionally, contact with low work function metal with strong electron affinity creates a strong build-in potential that facilitates the transportation of carriers and promises nearly unaffected drift current even under high external bias (region II in Fig. 1). As a consequence, an efficient device with a high FF value can be obtained.

In most of our discussion, we mentioned some examples dedicated to the selection and design of the electron transport layer as an approach to achieve high PCE and FF. It should be kept in mind that the selection and design of the hole transport layer is of equal importance. Different kinds of hole transport layers have been developed for OPVs, such as conducting polymers, conjugated polyelectrolytes, and metal oxides. A good coordination of both electron transport layer and hole transport layer can synergistically boost the FF and performance of OPVs. To give some ideas for designing better buffer layers, we organize examples of high FF OPVs with novel buffer layers in Table 1. A comprehensive discussion of the selection and design of buffer layers can be found in ref. 77–79 and 95–98.

4. Effects of BHJ features on the fill factor of OPVs

4.1. Domain size

The FF can be regarded as the decreased extent of device current resulting from the decline of a build-in potential across the device. When a device is under *J–V* characteristic test scanning from J_{sc} to V_{oc}, the build-in potential will gradually decrease due to the gradually increased external applied bias. Therefore, the current extracted from the device with a superior FF will change very little when the build-in potential drops a lot. This means that a high FF for a device can be achieved with efficient carrier extraction yield even under a small potential difference. In OPV, this can be obtained by fine-tuning the domain size to suppress the recombination rate.

OPVs are mostly composed of light elements such as C, N, O, H, S connected by covalent bonds. These materials generally exhibit low permeability in the range of 2–4, which are not high enough to screen the coulombic attraction force between photogenerated electron–hole pairs. Hence in OPVs, the exciton is tightly bound together with binding energy about 0.3–0.5 eV.[33,50] Unlike inorganic counterparts, the tightly bound exciton can't be separated into free carriers to contribute current by thermal iteration, but can only be set apart by a strong local electric field. Fortunately in OPVs, the local field at the interface between the donor and acceptor domain is strong enough to address this issue. Excitons originated in the donor domain may have a chance to diffuse toward the domain interface and dissociate into free carriers by the strong local field. In order to promote the dissociation rate and suppress geminate recombination, the domain size must be approximately the diffusion length of excitons to ensure that most excitons can reach the domain interface within their lifetime. The domain size can be tailored by varying the processing conditions, such as thermal treatment,[99,100] solvent vapor treatment,[101,102] high boiling point additive,[103–108] ternary blend,[109–115] *etc.*

The evolution of the nanostructure and domain size in OPVs is often qualitatively characterized by TEM and AFM or quantitatively analyzed by GISAXS and GIWAXS.[99,116–126] Fig. 6(a) and (b) show the KPFM and TEM images of PCPDTBT:$PC_{71}BM$,[104] a donor–acceptor type copolymer/fullerene BHJ system processed with or without high boiling additive DIO. In the same study, the nanostructure has also been probed by using GISAXS and GIWAXS techniques. In the cast film of PCPDTBT:$PC_{71}BM$ without a high boiling additive, $PC_{71}BM$ is loosely packed and its correlation length is quite large. This kind of large and loosely packed $PC_{71}BM$ domain inhibits the crystallization of its counterpart polymer, and presents an unfavorable condition for

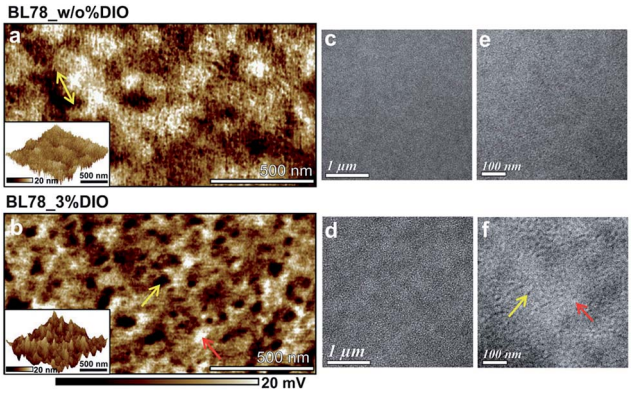

Fig. 6 KPFM (a) and TEM images (c and e) of the PCPDTBT:$PC_{71}BM$ thin film processed without DIO. KPFM (b) and TEM images (d and f) of the PCPDTBT:$PC_{71}BM$ thin film processed with DIO. The inset of each KPFM image is the corresponding AFM image. Reproduced with permission from ref. 104. © Royal Society.

exciton dissociation. This situation can be improved by addition of a small amount of DIO. DIO has a high boiling point and preferential solubility for $PC_{71}BM$. As a result, during the drying of the PCPDTBT:$PC_{71}BM$ cast film, the polymer would crystallize first and leave only a confined domain for $PC_{71}BM$ to occupy. Therefore, the nanostructure and the domain size can be effectively manipulated by this method. With an appropriate amount of DIO, the degree of crystallization of PCPDTBT can be enhanced while the domain of $PC_{71}BM$ can be constrained in the same scale of exciton diffusion length. As a result, compared to the device processed without DIO, the one containing the appropriate amount of DIO shows an over 25% increase of FF, from 44% to 56%.

4.2. Gradated BHJ

OPVs are considered as "excitonic solar cells". This means the characteristics of excitons – large exciton binding energy and limited exciton diffusion length – are critical variables in the design of materials and device architectures. Hence, the distinctive BHJ architecture can be employed to reduce the geminate recombination and to maximize the dissociation of excitons and output current. Nevertheless, the randomly distributed donor and acceptor phases in the BHJ inevitably create a chance that holes transported through the donor phase meet electrons transported through the acceptor phase before collected by the electrode, thus increasing the possibility of bimolecular recombination and reducing the device FF. In order to tackle this issue and to enhance the OPV performance, an ideal structure for OPVs is proposed: the ordered-BHJ (Fig. 7).[127–130] The ordered-BHJ consists of continuous and interdigitated donor and acceptor phases with domain width at the scale of 10 nm. Each ordered donor or acceptor phase is linked directly to its respective electrode, which can simultaneously maximize the exciton dissociation and minimize bimolecular recombination. Unfortunately, fabrication of an ideal ordered-BHJ is more difficult than a random BHJ. No effective method has been developed to date. However, the ordered-BHJ concept is so compelling that an alternative

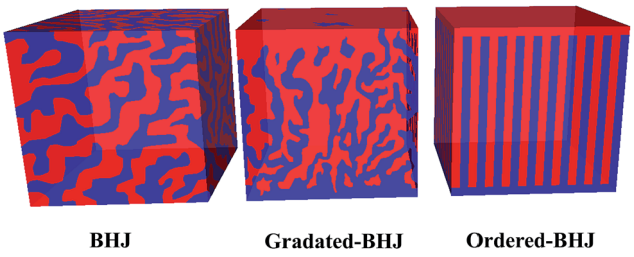

Fig. 7 Schematics of typical BHJ of OPV (left), gradated BHJ (middle) and the proposed ideal ordered-BHJ (right). Note that different colors stand for different domains of the donor and acceptor.

mimic, namely, gradated-BHJ, is proposed. The gradated-BHJ has a random distribution of donor and acceptor phases like the BHJ but contains a slight vertical phase separation with higher donor concentration near the anode and higher acceptor concentration near the cathode. This gradated-BHJ can be produced by self-assembly of molecules or surface modification of the substrate.[71,75,131] During the self-assembly process, if the affinity of the donor material to the substrate is better than that of the acceptor material, the concentration of the donor material may be higher near the substrate and the concentration of the acceptor material may be enriched on top. As a result, a vertically gradated BHJ is formed. The same argument is also valid when the acceptor material has better affinity to the substrate than the donor material, forming a gradated BHJ with the acceptor concentrated near the substrate (bottom) and the donor concentrated near the top.

Guo *et al.* reported highly ordered polymers with close π–π stacking distance.[132] Interestingly, these polymers showed less affinity to the ZnO thin film compared to $PC_{71}BM$. This affinity was examined by the contact angle and quantified by the spreading parameter. The authors took advantage of this special property and fabricated an inverted device with ZnO as the cathode buffer layer on the substrate. The resulting polymer:fullerene blend thin film showed a relatively higher $PC_{71}BM$ concentration near the ZnO side and a relatively higher polymer concentration near the top side of MoO_3. The as-fabricated device exhibits an exceptional FF near 80%, which is due to a close π–π stacking and a vertically gradated structure. Both attributes reduce bimolecular recombination and facilitate charge extraction.

The promising concept of gradated BHJ can also be obtained by post solvent treatment after the formation of the BHJ layer. Xiao *et al.* successfully modified the vertical composition distribution in various DIO-modified BHJ systems by methanol flux.[133] During the fabrication of the DIO-modified BHJ system, a small amount of DIO is added into the solution mixture of polymer and fullerene. The thin film morphology of the mixture can be controlled by taking advantage of the DIO's high boiling point and preferential solubility for fullerene, as discussed in the previous section. After the coating process, DIO will remain in the thin film for a long time to facilitate the aggregation of fullerene into nanoclusters. The post-treatment by methanol flux can bring these fullerene-containing nanoclusters upward and result in a gradated BHJ with the enriched acceptor on the

top and enriched donor on the bottom. In their experiments, by creating a desired gradated BHJ structure, an increase of FF at 18–22% can be realized.

4.3. π–π stacking distance

A good FF can be achieved when carriers are smoothly transported through the device with a minimum chance of recombination. As a result, it is critical to increase the conductivity of organic molecules and the as-fabricated BHJ. The conductivity of organic molecules originates from the conjugated π electrons. In the state-of-the-art OPV devices, fullerene derivatives are often chosen as the acceptor materials because of their excellent electron affinity and suitable energy level alignment. Therefore, the conductivity issue resides more often on the donor part.

Polymers and small molecules can orderly pack together and form crystallites when fabricated into a thin film. There are two kinds of packing direction. One is along the side chain direction; the other is along the normal of the planar conjugated ring. The former is often denoted as the [100] direction, and the later as [010]. Packing along [100] can be considered as interdigitation of the side chain, and packing along the [010] can be regarded as piling up of conjugated rings. Hence, the [010] direction is also stated as the π–π stacking direction, which emphasizes the π electrons on the conjugated rings. When transported through polymer crystallites, carriers are known to drift faster along [010] than along [100]. This phenomenon can be explained by both the shorter inter-molecular distance along [010] than along [100] and the existence of the non-conducting side chain as the transportation barrier. Therefore, the [010] direction is considered more seminal in terms of carrier conductivity.[134–139]

Theoretically, reducing the π–π stacking distance can promote the mobility of the as-prepared thin film and increase the FF of the OPV device. Indeed, there are reports to understand the relationship between the π–π stacking distance and FF. Szarko *et al.* investigated the issue by designing a series of polymers consisting of the same backbone to rule out any extraneous influential parameters.[140] The π–π stacking distance is manipulated by the side chain attached to the backbone.[141–145] The linear side chain takes little space and will not interfere with the stacking between molecules in the [010] direction, resulting in a smaller π–π stacking distance. The branched side chain is rather bulky and affects the stacking in the [010] direction, causing an increased π–π stacking distance. The GIWAXS study shows that the π–π stacking distance decreases from 3.89 to 3.65 Å for polymer thin films with branched *vs.* linear side chains. With a shorter stacking distance, the device FF is improved from below 45% to over 65% due to the increased carrier mobility.

4.4. π–π stacking direction

In conjugated molecules, charge carriers are transported between molecules by overlapped π orbitals. The π–π stacking distance determines the transporting speed, and the π–π stacking direction determines the transporting direction. Both features are crucial to the ability of charge extraction. For the π–π stacking distance, the shorter, the better, as discussed previously. For the π–π stacking direction, the direction provides a specific function. Its effect on charge extraction is more complex. For instance, if the material is designed to serve in thin film transistors, the π–π stacking direction parallel to the substrate is more desirable to improve the horizontal charge transport. On the other hand, if the material is designed to serve for OPVs, π–π stacking perpendicular to the substrate is more desirable to facilitate vertical charge transport.

In a conjugated molecular system, crystallites are shaped like a plate. The face of the plate is defined by the plane of the conjugated ring. The edge of the plate is occupied by the side chain. If the π–π stacking direction is parallel to the substrate, it is denoted as "edge-on" orientation (Fig. 8(a)). If the π–π stacking direction is normal to the substrate, it is denoted as "face-on" orientation (Fig. 8(b)). Sometimes it is possible that an azimuthal distribution of the π–π stacking direction, that is, a random mixing of edge-on and face-on orientations, can be beneficial to the 3-D charge transport in the complex nanostructure of the BHJ. Therefore, the FF can be enhanced with improvement of charge extraction by tailoring the π–π stacking direction.

Although the approaches and mechanism to control the π–π stacking direction are not straight-forward, recent papers report progress in the area.[146–153] Zhang *et al.* noticed that with the increase of side chain attachment density (*i.e.* the amount of side chains), both the solubility of the polymer and the proportion of the face-on orientation of the thin film increase.[152] Accordingly, they hypothesized a rule that the stacking direction can be modulated by side chain density. Some following studies also observed a similar trend.[147–151] Chen *et al.* proposed another approach to control the stacking direction. Their experiments show that when the co-planarity of the polymer backbone increases (*i.e.* linear conformation of the polymer chain), the polymer is more likely to form the face-on orientation.[146] From these studies, one can propose that increasing the side chain attachment density and co-planarity can tailor the molecular packing into face-on orientation. However, care should be taken that an excessive side chain density is deleterious to the accompanied issues such as low crystallinity, low absorption, low π-electron density, and synthesis difficulty.

Vohra *et al.* reported a unique polymer that forms "edge-on" orientation in the pristine polymer thin film, whereas it

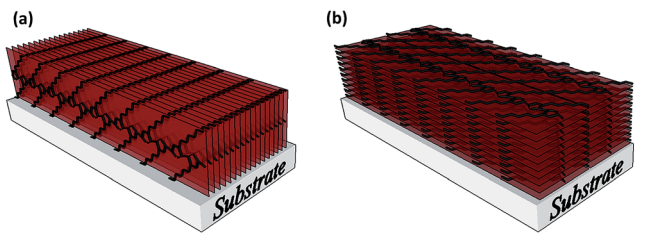

Fig. 8 Illustrations of (a) edge-on orientation and (b) face-on orientation.

transforms into "face-on" orientation when blended with fullerene derivatives.[154] This characteristic makes it favorable to transport charge carriers in OPVs. In addition, this polymer shows vertically dependent orientation in the polymer:fullerene film, with "edge-on" orientation dominating on the bottom and "face-on" orientation dominating on the top. Such uniquely mixed orientation makes it more efficient to collect holes on top than on bottom. As a consequence, efficient carrier transport and reduced bimolecular recombination can be simultaneously obtained. In summary, by optimizing molecular orientation, high crystallinity and short π–π stacking, a FF of nearly 75% can be achieved by an inverted architecture which collects electrons on the bottom and holes on the top.

4.5. Domain purity

The BHJ is generally formed by coating a solution containing both donor material and acceptor material. During the solvent drying process, the donor and acceptor material each will aggregate to some extent because of their miscibility and crystallinity,[155–158] leading to phase separation and creating a region with a higher concentration of the donor material and a region with a higher concentration of the acceptor material, which are termed as "donor rich domain" and "acceptor rich domain", respectively. As discussed in the previous section, an adequate domain size with the length scale comparable to the exciton diffusion length is beneficial to exciton dissociation and charge transport, thus leading to an improved FF. In this section we focus on the domain purity and find out how this feature influences the device FF.

The domain purity can be probed by the resonant soft X-ray scattering (R-SoXS) method.[125,159–164] By carefully choosing the photon energy to emphasize the material contrast, the total scattering intensity (TSI) of the scattering profile can quantitatively determine the domain contrast and give statistical significance to domain purity. The detailed introduction and working principle of this powerful technique can be found in the literature.[165,166]

Collins *et al.* have succeeded in quantitatively determining the domain purity by R-SoXS combined with resonant microscopy.[166] It is found that in the PTB7:$PC_{71}BM$ system, one of the most representative and successful BHJ systems discovered in recent years, the acceptor rich domain consists of nearly 100% $PC_{71}BM$. On the other hand, the donor rich domain only comprises about 70% PTB7 and 30% $PC_{71}BM$, which coincides with the thermodynamic miscibility of $PC_{71}BM$ in PTB7. This can be explained by the fact that, during the film drying process, PTB7 and $PC_{71}BM$ reach a thermodynamically stable condition, forming a matrix with composition equal to thermodynamic miscibility. The excess $PC_{71}BM$ separates out from the matrix and forms a domain with high purity. After the domain compositions are established, the high purity $PC_{71}BM$ domain in contact with the polymer chain in the PTB7 domain can promote exciton separation leading to a high FF and performance. Compared with the PTB7 domain in which $PC_{71}BM$ percolates into at the molecular level, the formation of pure $PC_{71}BM$ agglomerates in the $PC_{71}BM$ domain lowers its LUMO level and shows greater difference from the LUMO level of PTB7. The greater difference of LUMO levels between PTB7 and $PC_{71}BM$ increases the strength of the local field at the donor–acceptor interface and enhances the driving force of exciton separation. Therefore, high domain purity and a sharp domain interface can increase the interface potential difference and enhance the probability of exciton separation, leading to suppressed recombination and field-independent charge separation yield. This partially explains the high FF and PCE of the state-of-the-art PTB7:$PC_{71}BM$ system.

The previous paragraph mentions that the PTB7 donor domain contains only 70% PTB7. Therefore, one can speculate that further enhancing the PTB7 domain purity while maintaining the optimal domain size may improve the FF and PCE of state-of-the-art PTB7:$PC_{71}BM$ system. This can be achieved by a ternary blend system comprising two donor materials and one acceptor material.[167,168] Zhang *et al.* made a ternary system by adding a small molecule *p*-DTS(FBTTH$_2$)$_2$ of high crystalline tendency into PTB7-Th:$PC_{71}BM$.[20] When the blending ratio is less than 15 wt%, the added small molecule can form an alloy with PTB7-Th and increase its crystallinity. When the polymer has a high tendency to form ordered packing, the ability for $PC_{71}BM$ molecules to percolate into the donor domain decreases, hence the donor domain purity increases. This small molecule modification also reduces the π–π stacking distance in the donor domain. Both changes – increasing domain purity and shortening π–π stacking distance – enhance the exciton separation yield and charge transport ability, leading to a higher FF (from 65% to 75%) and PCE (from 9.2% to 10.5%).

From the above discussion, it can be deduced that the domain purity can be improved by increasing the miscibility difference and crystallinity of donor materials. Liu *et al.* developed a novel processing strategy and manipulated the crystallinity of the polymer in the BHJ by tailoring the polymer side chain and processing temperature.[19] They discovered that, with the 2-octyldodecyl alkyl chain attached to the thiophene unit, as shown in Fig. 9, the polymer is prone to aggregation and forms an ordered stacking structure in solution at room temperature. However this ordered stacking structure can be disrupted at relatively high temperatures such as 85 °C. This aggregation behavior is utilized to fabricate a "near ideal" BHJ morphology. At first, the polymer:fullerene blend solution is heated at a high temperature of 110 °C to prevent polymer aggregation and to form a nearly homogeneous blend in order to favor a small domain size. During the gradual cooling process, the polymer first coats on the substrate, and then begins to aggregate, crystallize and separate out of $PC_{71}BM$. All these delicate steps successfully lead to a high purity domain and small domain size. As a result, the OPV devices show an exceptional FF (>75%) and PCE (>10%).

After our discussions above, it is important to keep in mind that the FF is the consequence of a series of intricate physical events which begins from the exciton generation in the complicated BHJ structure and ends with the carrier collection by electrodes. Hence those devices with high values of FF often benefit from two or more BHJ features that are listed and discussed in this article. For example, in the work reported by Liu

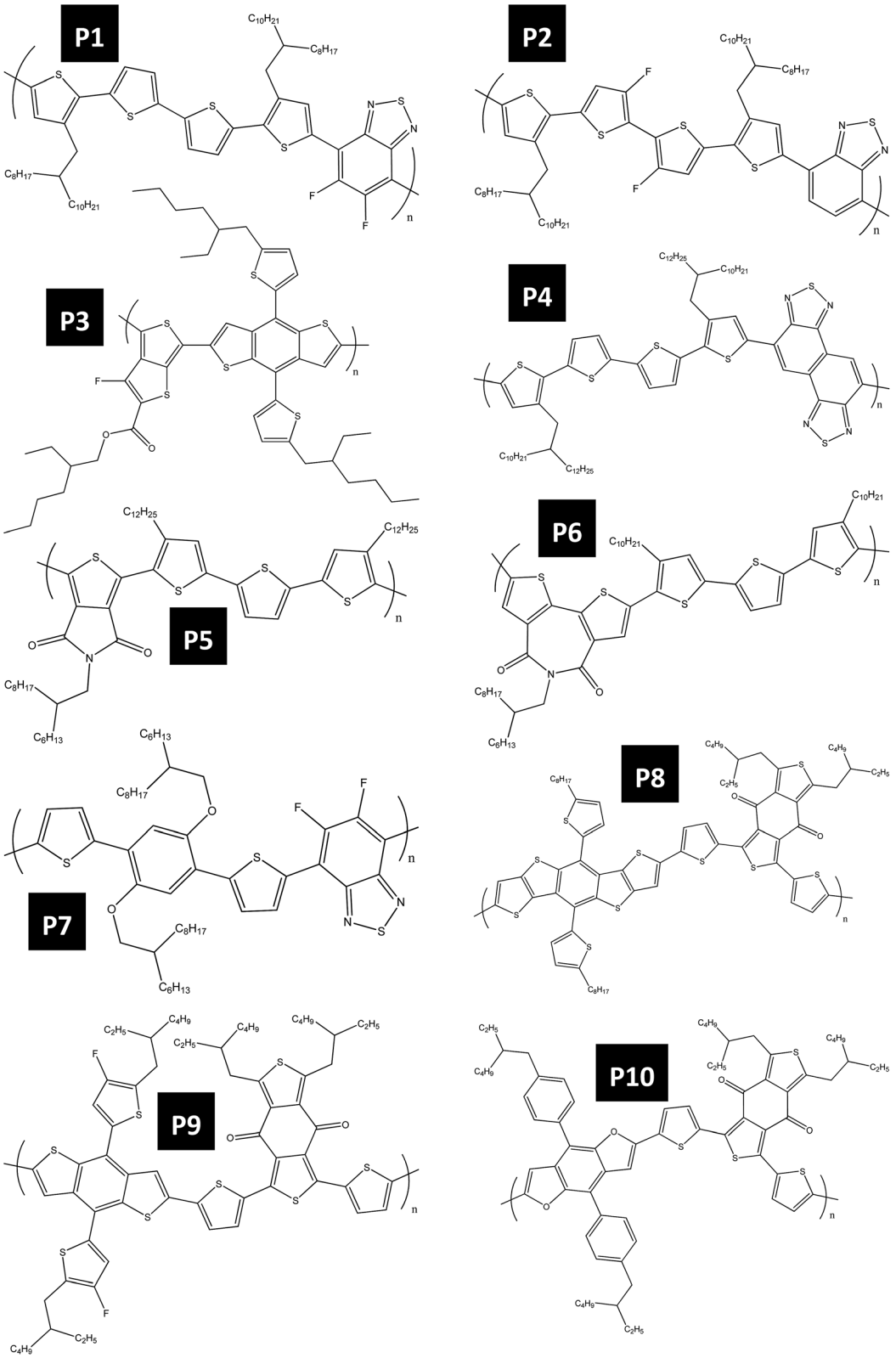

Fig. 9 Chemical structures of polymers for the BHJ with high FF and PCE.

et al.[19] temperature-dependent aggregation behavior is employed to attain properties including close π–π stacking distance, face-on π–π stacking orientation, and high domain purity, which synergistically promote the FF and PCE.[19] Fig. 9 and 10 show examples of recently discovered conducting polymers and small conjugated molecules with unique properties

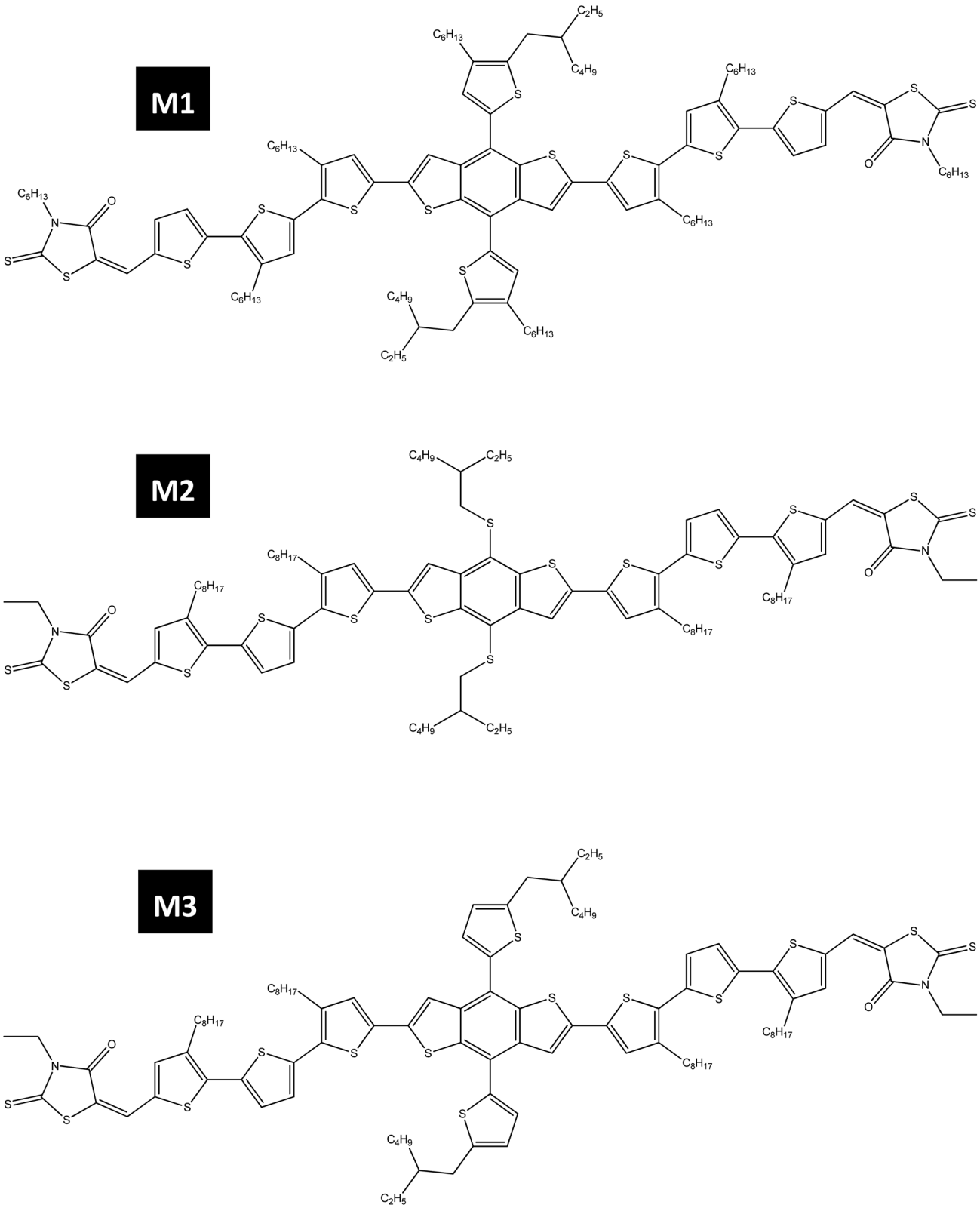

Fig. 10 Chemical structures of small molecules for the BHJ with high FF and PCE.

and features respectively. Table 2 summarizes the results using those materials to achieve high FF and PCE devices through different approaches to obtain critical BHJ features. The BHJ thickness is also listed to demonstrate that a thick BHJ layer does not always preclude a high FF as long as other BHJ features can benefit smooth charge transportation. Additionally, data

Table 2 Summary of BHJ features of high FF and PCE devices

BHJ	Thickness (nm)	FF (%)	PCE (%)	Domain size (nm)	Stacking distance (Å)	Stacking direction	Gradated	Domain purity	Ref.
P1:$TC_{71}BM$	300	75	10.8	30–40	3.54	Optimal	N/A	Optimal	19
P2:$PC_{71}BM$	300	74	10.4	30–40	3.54	Optimal	N/A	Optimal	19
P3:M4[a]:$PC_{71}BM$	100	75	10.5	10–15	3.63	Optimal	N/A	Optimal	20
P3:$PC_{71}BM$	100	73	10.6	10–15	3.63	N/A	N/A	N/A	22
P4:$PC_{71}BM$	290	73	10.1	N/A	3.5	Optimal, $A_{xy}/A_z \sim 0.8$	N/A	N/A	154
P5:$PC_{71}BM$	130	79	7.9	10–20	3.62	>14	Optimal	Optimal	132 and 169
P6:$PC_{71}BM$	120	77	8.6	10–20	3.56	14	Optimal	Optimal	132 and 169
P7:$PC_{71}BM$	290	73	9.3	Optimal, fibrillary network	3.57–3.59	N/A	N/A	N/A	170
P8:$PC_{71}BM$	100	75	9.7	Optimal, fibrillary network	N/A	N/A	N/A	N/A	89
P9:$PC_{71}BM$	75	74	9.2	Optimal, fibrillary network	3.78 (neat polymer)	N/A	N/A	Optimal	171
P10:$PC_{71}BM$	150	77	9.4	20–40	3.67	N/A	N/A	N/A	172
M1:$PC_{71}BM$	250	77	9.3	Optimal	3.60	Azimuthal	N/A	N/A	173
M2:$PC_{71}BM$	120	73	9.9	15	3.61	Azimuthal	N/A	N/A	88 and 174
M3:$PC_{71}BM$	N/A	76	9.5	30–40	3.62	Azimuthal	N/A	Optimal	90

[a] M4 indicates small molecule *p*-DTS($FBTTH_2$)$_2$.

and devices shown in both Tables 1 and 2 demonstrate that top-performing OPVs can be made by optimizing selected buffer layers and desired BHJ features. In summary, we see numerous and productive opportunities for further progress in OPV materials and device design to achieve a high FF.

5. Conclusion

In this review, we emphasize on the third parameter, FF, that can have a great influence on the PCE of OPVs. Because of the complex device structure formed by the BHJ and complicated photon–charge carrier conversion mechanism, this parameter is more abstract than the other parameters determining PCE, *i.e.*, V_{oc} and J_{sc}. We first derive the mathematical equations that show how the parasitic resistance, R_s and R_{sh}, and diode ideality factor, n, change the device FF. At the same time, we discuss the FF in a theoretical and physical manner. We then examine the FF from the viewpoint of a device or material designer and discuss some of the important device and BHJ features that show promise in obtaining a high FF, including preventing shorting, buffer layer, domain size, gradated BHJ, π–π stacking distance, π–π stacking direction, and domain purity. For a long time, the FF is considered as the weak point that hinders OPVs from outperforming their inorganic counterparts, and it is thought that making a thick layer of BHJ to increase the photon absorption yield often reduces the FF because of the increased recombination probability. However, by optimizing the features described above, there are more and more OPV devices with BHJ thickness reaching 300 nm while exhibiting attractive FFs comparable to those of inorganic solar cells. In this review, we clarify the vague concept of the FF of OPVs and provide feasible approaches to further enhance the FF and PCE of OPVs.

Acknowledgements

Financial support from the Ministry of Science and Technology of Taiwan (MOST 104-3113-E-002-010) is highly appreciated. Editing of this manuscript by Dr Margaret M. S. Wu, Emeritus Senior Scientific Advisor of ExxonMobil Research and Engineering Co., is highly appreciated.

References

1 T. R. Andersen, H. F. Dam, M. Hösel, M. Helgesen, J. E. Carlé, T. T. Larsen-Olsen, S. A. Gevorgyan, J. W. Andreasen, J. Adams, N. Li, F. Machui, G. D. Spyropoulos, T. Ameri, N. Lemaître, M. Legros, A. Scheel, D. Gaiser, K. Kreul, S. Berny, O. R. Lozman, S. Nordman, M. Välimäki, M. Vilkman, R. R. Søndergaard, M. Jørgensen, C. J. Brabec and F. C. Krebs, *Energy Environ. Sci.*, 2014, **7**, 2925.

2 N. Espinosa, M. Hösel, M. Jørgensen and F. C. Krebs, *Energy Environ. Sci.*, 2014, **7**, 855.

3 F. Guo, T. Ameri, K. Forberich and C. J. Brabec, *Polym. Int.*, 2013, **62**, 1408–1412.

4 F. C. Krebs, N. Espinosa, M. Hösel, R. R. Søndergaard and M. Jørgensen, *Adv. Mater.*, 2014, **26**, 29–39.

5 R. Søndergaard, M. Hösel, D. Angmo, T. T. Larsen-Olsen and F. C. Krebs, *Mater. Today*, 2012, **15**, 36–49.

6 S. Lizin, S. Van Passel, E. De Schepper, W. Maes, L. Lutsen, J. Manca and D. Vanderzande, *Energy Environ. Sci.*, 2013, **6**, 3136.

7 T. R. Andersen, H. F. Dam, B. Andreasen, M. Hösel, M. V. Madsen, S. A. Gevorgyan, R. R. Søndergaard, M. Jørgensen and F. C. Krebs, *Sol. Energy Mater. Sol. Cells*, 2014, **120**, 735–743.

8 Z. M. Beiley and M. D. McGehee, *Energy Environ. Sci.*, 2012, **5**, 9173.
9 S. B. Darling and F. You, *RSC Adv.*, 2013, **3**, 17633.
10 N. Espinosa, M. Hösel, D. Angmo and F. C. Krebs, *Energy Environ. Sci.*, 2012, **5**, 5117–5132.
11 R. Po, A. Bernardi, A. Calabrese, C. Carbonera, G. Corso and A. Pellegrino, *Energy Environ. Sci.*, 2014, **7**, 925.
12 N. Espinosa, F. O. Lenzmann, S. Ryley, D. Angmo, M. Hösel, R. R. Søndergaard, D. Huss, S. Dafinger, S. Gritsch, J. M. Kroon, M. Jørgensen and F. C. Krebs, *J. Mater. Chem. A*, 2013, **1**, 7037.
13 C. Koidis, S. Logothetidis, A. Ioakeimidis, A. Laskarakis and C. Kapnopoulos, *Org. Electron.*, 2013, **14**, 1744–1748.
14 T. Chen, L. Qiu, Z. Yang and H. Peng, *Chem. Soc. Rev.*, 2013, **42**, 5031.
15 Y. Liang and L. Yu, *Acc. Chem. Res.*, 2010, **43**, 1227–1236.
16 S.-H. Yang, C.-S. Hsu and Y.-J. Cheng, *Chem. Rev.*, 2009, **109**, 5868–5923.
17 M. C. Scharber, D. Mühlbacher, M. Koppe, P. Denk, C. Waldauf, A. J. Heeger and C. J. Brabec, *Adv. Mater.*, 2006, **18**, 789–794.
18 H. Zhou, L. Yang, S. Stoneking and W. You, *ACS Appl. Mater. Interfaces*, 2010, **2**, 1377–1383.
19 Y. Liu, J. Zhao, Z. Li, C. Mu, W. Ma, H. Hu, K. Jiang, H. Lin, H. Ade and H. Yan, *Nat. Commun.*, 2014, **5**, 5293.
20 J. Zhang, Y. Zhang, J. Fang, K. Lu, Z. Wang, W. Ma and Z. Wei, *J. Am. Chem. Soc.*, 2015, **137**, 8176–8183.
21 J. D. Chen, C. Cui, Y. Q. Li, L. Zhou, Q. D. Ou, C. Li, Y. Li and J. X. Tang, *Adv. Mater.*, 2015, **27**, 1035–1041.
22 Z. He, B. Xiao, F. Liu, H. Wu, Y. Yang, S. Xiao, C. Wang, T. P. Russell and Y. Cao, *Nat. Photonics*, 2015, **9**, 174–179.
23 H. Hu, K. Jiang, G. Yang, J. Liu, Z. Li, H. Lin, Y. Liu, J. Zhao, J. Zhang, F. Huang, Y. Qu, W. Ma and H. Yan, *J. Am. Chem. Soc.*, 2015, **137**, 14149–14157.
24 B. Kan, M. Li, Q. Zhang, F. Liu, X. Wan, Y. Wang, W. Ni, G. Long, X. Yang, H. Feng, Y. Zuo, M. Zhang, F. Huang, Y. Cao, T. P. Russell and Y. Chen, *J. Am. Chem. Soc.*, 2015, **137**, 3886–3893.
25 J. Zhao, Y. Li, G. Yang, K. Jiang, H. Lin, H. Ade, W. Ma and H. Yan, *Nat. Energy*, 2016, **1**, 15027.
26 C. C. Chen, W. H. Chang, K. Yoshimura, K. Ohya, J. You, J. Gao, Z. Hong and Y. Yang, *Adv. Mater.*, 2014, **26**, 5670–5677.
27 N. Li and C. J. Brabec, *Energy Environ. Sci.*, 2015, **8**, 2902–2909.
28 H. Zhou, Y. Zhang, C. K. Mai, S. D. Collins, G. C. Bazan, T. Q. Nguyen and A. J. Heeger, *Adv. Mater.*, 2015, **27**, 1767–1773.
29 S. H. Park, A. Roy, S. Beaupré, S. Cho, N. Coates, J. S. Moon, D. Moses, M. Leclerc, K. Lee and A. J. Heeger, *Nat. Photonics*, 2009, **3**, 297–302.
30 J. Yan, G. Luo, B. Xiao, H. Wu, Z. He and Y. Cao, *Org. Electron.*, 2015, **24**, 125–130.
31 S. Foster, F. Deledalle, A. Mitani, T. Kimura, K.-B. Kim, T. Okachi, T. Kirchartz, J. Oguma, K. Miyake, J. R. Durrant, S. Doi and J. Nelson, *Adv. Energy Mater.*, 2014, **4**, 1400311.
32 T. Strobel, V. Dyakonov and C. Deibel, *Adv. Mater.*, 2010, **22**, 4097–4111.
33 K. Feron, W. J. Belcher, C. J. Fell and P. C. Dastoor, *Int. J. Mol. Sci.*, 2012, **13**, 17019–17047.
34 R. A. Janssen and J. Nelson, *Adv. Mater.*, 2013, **25**, 1847–1858.
35 Y.-W. Su, S.-C. Lan and K.-H. Wei, *Mater. Today*, 2012, **15**, 554–562.
36 J. J. M. Halls, K. Pichler, R. H. Friend, S. C. Moratti and A. B. Holmes, *Appl. Phys. Lett.*, 1996, **68**, 3120.
37 O. V. Mikhnenko, H. Azimi, M. Scharber, M. Morana, P. W. M. Blom and M. A. Loi, *Energy Environ. Sci.*, 2012, **5**, 6960.
38 J. C. Blakesley and D. Neher, *Phys. Rev. B: Condens. Matter Mater. Phys.*, 2011, **84**, 075210.
39 D. Credgington and J. R. Durrant, *J. Phys. Chem. Lett.*, 2012, **3**, 1465–1478.
40 B. Qi and J. Wang, *J. Mater. Chem.*, 2012, **22**, 24315.
41 W. Tress, K. Leo and M. Riede, *Adv. Funct. Mater.*, 2011, **21**, 2140–2149.
42 N. C. Giebink, G. P. Wiederrecht, M. R. Wasielewski and S. R. Forrest, *Phys. Rev. B: Condens. Matter Mater. Phys.*, 2010, **82**, 155305.
43 A. Foertig, J. Rauh, V. Dyakonov and C. Deibel, *Phys. Rev. B: Condens. Matter Mater. Phys.*, 2012, **86**, 115302.
44 M. A. Green, *Solid-State Electron.*, 1981, **24**, 788–789.
45 W. G. T. Aernouts, J. Poortmans, P. Heremans, S. Borghs and R. Mertens, *Thin Solid Films*, 2002, **403–404**, 297–301.
46 J. D. Servaites, M. A. Ratner and T. J. Marks, *Energy Environ. Sci.*, 2011, **4**, 4410.
47 L. Wu, H. Zang, Y.-C. Hsiao, X. Zhang and B. Hu, *Appl. Phys. Lett.*, 2014, **104**, 153903.
48 J. D. Servaites, M. A. Ratner and T. J. Marks, *Appl. Phys. Lett.*, 2009, **95**, 163302.
49 J. Cornil, J. J. M. Halls, D. A. d. Santos, R. Silbey, D.-H. Hwang, A. B. Holmes, J. L. Brédas and R. H. Friend, *Phys. Rev. B: Condens. Matter Mater. Phys.*, 1999, **60**, 5721–5727.
50 T. M. Clarke and J. R. Durrant, *Chem. Rev.*, 2010, **110**, 6736–6767.
51 G. del Pozo, B. Romero and B. Arredondo, *Sol. Energy Mater. Sol. Cells*, 2012, **104**, 81–86.
52 B. Y. Finck and B. J. Schwartz, *Appl. Phys. Lett.*, 2013, **103**, 053306.
53 J. D. Servaites, S. Yeganeh, T. J. Marks and M. A. Ratner, *Adv. Funct. Mater.*, 2010, **20**, 97–104.
54 B. Qi and J. Wang, *Phys. Chem. Chem. Phys.*, 2013, **15**, 8972–8982.
55 C. Duan, F. Huang and Y. Cao, *Polym. Chem.*, 2015, **6**, 8081–8098.
56 J.-Y. Lee, P. Peumans and W. Gaynor, *ACS Nano*, 2010, **4**, 30–34.
57 C.-H. C. R. Zhu, K. C. Cha, W. Yang, Y. B. Zheng, H. Zhou, T.-B. Song, C.-C. Chen, P. S. Weiss, G. Li and Y. Yang, *ACS Nano*, 2011, **5**, 9877–9882.
58 H. S. K. L. Hu, J.-Y. Lee, P. Peumans and Y. Cui, *ACS Nano*, 2010, **4**, 2955–2963.

59 W. Gaynor, G. F. Burkhard, M. D. McGehee and P. Peumans, *Adv. Mater.*, 2011, **23**, 2905–2910.
60 W. Gaynor, S. Hofmann, M. G. Christoforo, C. Sachse, S. Mehra, A. Salleo, M. D. McGehee, M. C. Gather, B. Lussem, L. Muller-Meskamp, P. Peumans and K. Leo, *Adv. Mater.*, 2013, **25**, 4006–4013.
61 Z. Yu, L. Li, Q. Zhang, W. Hu and Q. Pei, *Adv. Mater.*, 2011, **23**, 4453–4457.
62 D. Y. Choi, H. W. Kang, H. J. Sung and S. S. Kim, *Nanoscale*, 2013, **5**, 977–983.
63 S. Nam, M. Song, D. H. Kim, B. Cho, H. M. Lee, J. D. Kwon, S. G. Park, K. S. Nam, Y. Jeong, S. H. Kwon, Y. C. Park, S. H. Jin, J. W. Kang, S. Jo and C. S. Kim, *Sci. Rep.*, 2014, **4**, 4788.
64 D. S. Leem, A. Edwards, M. Faist, J. Nelson, D. D. Bradley and J. C. de Mello, *Adv. Mater.*, 2011, **23**, 4371–4375.
65 S. Trost, K. Zilberberg, A. Behrendt and T. Riedl, *J. Mater. Chem.*, 2012, **22**, 16224.
66 I. Hancox, L. A. Rochford, D. Clare, M. Walker, J. J. Mudd, P. Sullivan, S. Schumann, C. F. McConville and T. S. Jones, *J. Phys. Chem. C*, 2013, **117**, 49–57.
67 J. Subbiah, C. M. Amb, I. Irfan, Y. Gao, J. R. Reynolds and F. So, *ACS Appl. Mater. Interfaces*, 2012, **4**, 866–870.
68 K. Zilberberg, H. Gharbi, A. Behrendt, S. Trost and T. Riedl, *ACS Appl. Mater. Interfaces*, 2012, **4**, 1164–1168.
69 Z. Lu, C. Zhan, X. Yu, W. He, H. Jia, L. Chen, A. Tang, J. Huang and J. Yao, *J. Mater. Chem.*, 2012, **22**, 23492–23496.
70 K. M. O'Malley, C.-Z. Li, H.-L. Yip and A. K. Y. Jen, *Adv. Energy Mater.*, 2012, **2**, 82–86.
71 J. J. Intemann, K. Yao, Y.-X. Li, H.-L. Yip, Y.-X. Xu, P.-W. Liang, C.-C. Chueh, F.-Z. Ding, X. Yang, X. Li, Y. Chen and A. K. Y. Jen, *Adv. Funct. Mater.*, 2014, **24**, 1465–1473.
72 D. Gupta, M. Bag and K. S. Narayan, *Appl. Phys. Lett.*, 2008, **92**, 093301.
73 T. Shi, X. Zhu, D. Yang, Y. Xie, J. Zhang and G. Tu, *Appl. Phys. Lett.*, 2012, **101**, 161602.
74 V. Gupta, A. K. Kyaw, D. H. Wang, S. Chand, G. C. Bazan and A. J. Heeger, *Sci. Rep.*, 2013, **3**, 1965.
75 C. Y. Chang, C. E. Wu, S. Y. Chen, C. Cui, Y. J. Cheng, C. S. Hsu, Y. L. Wang and Y. Li, *Angew. Chem., Int. Ed.*, 2011, **50**, 9386–9390.
76 S. H. Liao, H. J. Jhuo, P. N. Yeh, Y. S. Cheng, Y. L. Li, Y. H. Lee, S. Sharma and S. A. Chen, *Sci. Rep.*, 2014, **4**, 6813.
77 H.-L. Yip and A. K. Y. Jen, *Energy Environ. Sci.*, 2012, **5**, 5994.
78 E. L. Ratcliff, B. Zacher and N. R. Armstrong, *J. Phys. Chem. Lett.*, 2011, **2**, 1337–1350.
79 S. Chen, J. R. Manders, S.-W. Tsang and F. So, *J. Mater. Chem.*, 2012, **22**, 24202.
80 Y. Zhou, J. W. Shim, C. Fuentes-Hernandez, A. Sharma, K. A. Knauer, A. J. Giordano, S. R. Marder and B. Kippelen, *Phys. Chem. Chem. Phys.*, 2012, **14**, 12014–12021.
81 J. J. Jasieniak, J. Seifter, J. Jo, T. Mates and A. J. Heeger, *Adv. Funct. Mater.*, 2012, **22**, 2594–2605.
82 D. Y. Kim, J. Subbiah, G. Sarasqueta, F. So, H. Ding, Irfan and Y. Gao, *Appl. Phys. Lett.*, 2009, **95**, 093304.
83 D. Fernández-Hevia, J. de Frutos, A. C. Caballero and J. F. Fernández, *J. Appl. Phys.*, 2002, **92**, 2890.
84 R. T. Tung, *Mater. Sci. Eng., R*, 2001, **35**, 1–138.
85 J.-C. Wang, C.-Y. Lu, J.-L. Hsu, M.-K. Lee, Y.-R. Hong, T.-P. Perng, S.-F. Horng and H.-F. Meng, *J. Mater. Chem.*, 2011, **21**, 5723.
86 Y. Zhou, C. Fuentes-Hernandez, J. W. Shim, T. M. Khan and B. Kippelen, *Energy Environ. Sci.*, 2012, **5**, 9827.
87 Y. Zhou, C. Fuentes-Hernandez, J. Shim, J. Meyer, A. J. Giordano, H. Li, P. Winget, T. Papadopoulos, H. Cheun, J. Kim, M. Fenoll, A. Dindar, W. Haske, E. Najafabadi, T. M. Khan, H. Sojoudi, S. Barlow, S. Graham, J. L. Bredas, S. R. Marder, A. Kahn and B. Kippelen, *Science*, 2012, **336**, 327–332.
88 B. Kan, Q. Zhang, M. Li, X. Wan, W. Ni, G. Long, Y. Wang, X. Yang, H. Feng and Y. Chen, *J. Am. Chem. Soc.*, 2014, **136**, 15529–15532.
89 L. Huo, T. Liu, X. Sun, Y. Cai, A. J. Heeger and Y. Sun, *Adv. Mater.*, 2015, **27**, 2938–2944.
90 M. Li, F. Liu, X. Wan, W. Ni, B. Kan, H. Feng, Q. Zhang, X. Yang, Y. Wang, Y. Zhang, Y. Shen, T. P. Russell and Y. Chen, *Adv. Mater.*, 2015, **27**, 6296–6302.
91 C. Duan, K. Zhang, X. Guan, C. Zhong, H. Xie, F. Huang, J. Chen, J. Peng and Y. Cao, *Chem. Sci.*, 2013, **4**, 1298.
92 S. H. Liao, Y. L. Li, T. H. Jen, Y. S. Cheng and S. A. Chen, *J. Am. Chem. Soc.*, 2012, **134**, 14271–14274.
93 Z. A. Tan, L. J. Li, F. Z. Wang, Q. Xu, S. S. Li, G. Sun, X. H. Tu, X. L. Hou, J. H. Hou and Y. F. Li, *Adv. Energy Mater.*, 2014, **4**, 1300884.
94 K. Zhang, C. Zhong, S. Liu, C. Mu, Z. Li, H. Yan, F. Huang and Y. Cao, *ACS Appl. Mater. Interfaces*, 2014, **6**, 10429–10435.
95 C. Duan, K. Zhang, C. Zhong, F. Huang and Y. Cao, *Chem. Soc. Rev.*, 2013, **42**, 9071–9104.
96 C.-C. Chueh, C.-Z. Li and A. K. Y. Jen, *Energy Environ. Sci.*, 2015, **8**, 1160–1189.
97 R. Steim, F. R. Kogler and C. J. Brabec, *J. Mater. Chem.*, 2010, **20**, 2499.
98 T.-H. Lai, S.-W. Tsang, J. R. Manders, S. Chen and F. So, *Mater. Today*, 2013, **16**, 424–432.
99 H. C. Liao, C. S. Tsao, T. H. Lin, C. M. Chuang, C. Y. Chen, U. S. Jeng, C. H. Su, Y. F. Chen and W. F. Su, *J. Am. Chem. Soc.*, 2011, **133**, 13064–13073.
100 G. Li, V. Shrotriya, J. Huang, Y. Yao, T. Moriarty, K. Emery and Y. Yang, *Nat. Mater.*, 2005, **4**, 864–868.
101 F. S. Fischer, D. Trefz, J. Back, N. Kayunkid, B. Tornow, S. Albrecht, K. G. Yager, G. Singh, A. Karim, D. Neher, M. Brinkmann and S. Ludwigs, *Adv. Mater.*, 2015, **27**, 1223–1228.
102 H. C. Liao, C. S. Tsao, Y. C. Huang, M. H. Jao, K. Y. Tien, C. M. Chuang, C. Y. Chen, C. J. Su, U. S. Jeng, Y. F. Chen and W. F. Su, *RSC Adv.*, 2014, **4**, 6246.
103 C.-C. Ho, C.-A. Chen, C.-Y. Chang, S. B. Darling and W.-F. Su, *J. Mater. Chem. A*, 2014, **2**, 8026–8032.
104 H.-C. Liao, C.-S. Tsao, Y.-T. Shao, S.-Y. Chang, Y.-C. Huang, C.-M. Chuang, T.-H. Lin, C.-Y. Chen, C.-J. Su, U. S. Jeng, Y.-F. Chen and W.-F. Su, *Energy Environ. Sci.*, 2013, **6**, 1938.

105 H.-C. Liao, C.-C. Ho, C.-Y. Chang, M.-H. Jao, S. B. Darling and W.-F. Su, *Mater. Today*, 2013, **16**, 326–336.
106 F. Etzold, I. A. Howard, N. Forler, D. M. Cho, M. Meister, H. Mangold, J. Shu, M. R. Hansen, K. Mullen and F. Laquai, *J. Am. Chem. Soc.*, 2012, **134**, 10569–10583.
107 T. Salim, L. H. Wong, B. Bräuer, R. Kukreja, Y. L. Foo, Z. Bao and Y. M. Lam, *J. Mater. Chem.*, 2011, **21**, 242–250.
108 W. L. Ma, J. K. Lee, C. J. Brabec, J. Yuen, Ji S. Moon, J. Y. Kim, K. Lee, G. C. Bazan and A. J. Heeger, *J. Am. Chem. Soc.*, 2008, **130**, 3619–3623.
109 Y. Zhang, D. Deng, K. Lu, J. Zhang, B. Xia, Y. Zhao, J. Fang and Z. Wei, *Adv. Mater.*, 2015, **27**, 1071–1076.
110 M. G. Murali, A. D. Rao, S. Yadav and P. C. Ramamurthy, *Polym. Chem.*, 2015, **6**, 962–972.
111 C.-S. T. H.-C. Liao, T.-H. Lin, M.-H. Jao, C.-M. Chuang, S.-Y. Chang, Y.-C. Huang, Y.-T. Shao, C.-Y. Chen, C.-J. Su, U.-S. Jeng, Y.-F. Chen and W.-F. Su, *ACS Nano*, 2012, **6**, 1657–1666.
112 H.-C. Liao, P.-H. Chen, R. Chang and W.-F. Su, *Polymers*, 2014, **6**, 2784–2802.
113 Y. Gu, C. Wang, F. Liu, J. Chen, O. E. Dyck, G. Duscher and T. P. Russell, *Energy Environ. Sci.*, 2014, **7**, 3782–3790.
114 Y. Yang, W. Chen, L. Dou, W.-H. Chang, H.-S. Duan, B. Bob, G. Li and Y. Yang, *Nat. Photonics*, 2015, **9**, 190–198.
115 Q. An, F. Zhang, J. Zhang, W. Tang, Z. Deng and B. Hu, *Energy Environ. Sci.*, 2016, **9**, 281–322.
116 H.-C. Liao, C.-S. Tsao, T.-H. Lin, M.-H. Jao, C.-M. Chuang, S.-Y. Chang, Y.-C. Huang, Y.-T. Shao, C.-Y. Chen, C.-J. Su, U.-S. Jeng, Y.-F. Chen and W.-F. Su, *ACS Nano*, 2012, **6**, 1657–1666.
117 C. Y. Chen, C. S. Tsao, Y. C. Huang, H. W. Liu, W. Y. Chiu, C. M. Chuang, U. S. Jeng, C. J. Su, W. R. Wu, W. F. Su and L. Wang, *Nanoscale*, 2013, **5**, 7629–7638.
118 M. Y. Chiu, U. S. Jeng, C. H. Su, K. S. Liang and K. H. Wei, *Adv. Mater.*, 2008, **20**, 2573–2578.
119 J. Gao, W. Chen, L. Dou, C. C. Chen, W. H. Chang, Y. Liu, G. Li and Y. Yang, *Adv. Mater.*, 2014, **26**, 3142–3147.
120 W. Wang, C. J. Schaffer, L. Song, V. Körstgens, S. Pröller, E. D. Indari, T. Wang, A. Abdelsamie, S. Bernstorff and P. Müller-Buschbaum, *J. Mater. Chem. A*, 2015, **3**, 8324–8331.
121 D. M. DeLongchamp, R. J. Kline and A. Herzing, *Energy Environ. Sci.*, 2012, **5**, 5980.
122 D. Wang, F. Liu, N. Yagihashi, M. Nakaya, S. Ferdous, X. Liang, A. Muramatsu, K. Nakajima and T. P. Russell, *Nano Lett.*, 2014, **14**, 5727–5732.
123 P. Muller-Buschbaum, *Adv. Mater.*, 2014, **26**, 7692–7709.
124 W. Chen, T. Xu, F. He, W. Wang, C. Wang, J. Strzalka, Y. Liu, J. Wen, D. J. Miller, J. Chen, K. Hong, L. Yu and S. B. Darling, *Nano Lett.*, 2011, **11**, 3707–3713.
125 W. Chen, M. P. Nikiforov and S. B. Darling, *Energy Environ. Sci.*, 2012, **5**, 8045.
126 F. Liu, S. Ferdous, E. Schaible, A. Hexemer, M. Church, X. Ding, C. Wang and T. P. Russell, *Adv. Mater.*, 2015, **27**, 886–891.
127 J. Weickert, R. B. Dunbar, H. C. Hesse, W. Wiedemann and L. Schmidt-Mende, *Adv. Mater.*, 2011, **23**, 1810–1828.
128 M. Wang and F. Wudl, *J. Mater. Chem.*, 2012, **22**, 24297.
129 F. Liu, Y. Gu, J. W. Jung, W. H. Jo and T. P. Russell, *J. Polym. Sci., Part B: Polym. Phys.*, 2012, **50**, 1018–1044.
130 T. R. Foong, K. L. Chan and X. Hu, *Nanoscale*, 2012, **4**, 478–485.
131 Y.-J. Cheng, C.-H. Hsieh, Y. He, C.-S. Hsu and Y. Li, *J. Am. Chem. Soc.*, 2010, **132**, 17381–17383.
132 X. Guo, N. Zhou, S. J. Lou, J. Smith, D. B. Tice, J. W. Hennek, R. P. Ortiz, J. T. L. Navarrete, S. Li, J. Strzalka, L. X. Chen, R. P. H. Chang, A. Facchetti and T. J. Marks, *Nat. Photonics*, 2013, **7**, 825–833.
133 Z. Xiao, Y. Yuan, B. Yang, J. VanDerslice, J. Chen, O. Dyck, G. Duscher and J. Huang, *Adv. Mater.*, 2014, **26**, 3068–3075.
134 D. H. Kim, J. T. Han, Y. D. Park, Y. Jang, J. H. Cho, M. Hwang and K. Cho, *Adv. Mater.*, 2006, **18**, 719–723.
135 T. W. Lee, D. H. Lee, J. Shin, M. J. Cho and D. H. Choi, *Polym. Chem.*, 2015, **6**, 1777–1785.
136 C. J. Mueller, E. Gann, C. R. McNeill and M. Thelakkat, *J. Mater. Chem. C*, 2015, **3**, 8916–8925.
137 K.-Y. Wu, C.-C. Chiu, W.-T. Chuang, C.-L. Wang and C.-S. Hsu, *Polym. Chem.*, 2015, **6**, 1309–1315.
138 Z. Yi, S. Wang and Y. Liu, *Adv. Mater.*, 2015, **27**, 3589–3606.
139 L. Zhai, S. I. Khondaker, J. Thomas, C. Shen and M. McInnis, *Nano Today*, 2014, **9**, 705–721.
140 J. M. Szarko, J. Guo, Y. Liang, B. Lee, B. S. Rolczynski, J. Strzalka, T. Xu, S. Loser, T. J. Marks, L. Yu and L. X. Chen, *Adv. Mater.*, 2010, **22**, 5468–5472.
141 Y. J. Hwang, T. Earmme, S. Subramaniyan and S. A. Jenekhe, *Chem. Commun.*, 2014, **50**, 10801–10804.
142 C. K. Mai, R. A. Schlitz, G. M. Su, D. Spitzer, X. Wang, S. L. Fronk, D. G. Cahill, M. L. Chabinyc and G. C. Bazan, *J. Am. Chem. Soc.*, 2014, **136**, 13478–13481.
143 J. Mei and Z. Bao, *Chem. Mater.*, 2014, **26**, 604–615.
144 T. Qin, W. Zajaczkowski, W. Pisula, M. Baumgarten, M. Chen, M. Gao, G. Wilson, C. D. Easton, K. Mullen and S. E. Watkins, *J. Am. Chem. Soc.*, 2014, **136**, 6049–6055.
145 H. Zhong, Z. Li, E. Buchaca-Domingo, S. Rossbauer, S. E. Watkins, N. Stingelin, T. D. Anthopoulos and M. Heeney, *J. Mater. Chem. A*, 2013, **1**, 14973.
146 M. S. Chen, J. R. Niskala, D. A. Unruh, C. K. Chu, O. P. Lee and J. M. J. Fréchet, *Chem. Mater.*, 2013, **25**, 4088–4096.
147 C. Cabanetos, A. El Labban, J. A. Bartelt, J. D. Douglas, W. R. Mateker, J. M. Frechet, M. D. McGehee and P. M. Beaujuge, *J. Am. Chem. Soc.*, 2013, **135**, 4656–4659.
148 M. S. Chen, O. P. Lee, J. R. Niskala, A. T. Yiu, C. J. Tassone, K. Schmidt, P. M. Beaujuge, S. S. Onishi, M. F. Toney, A. Zettl and J. M. Frechet, *J. Am. Chem. Soc.*, 2013, **135**, 19229–19236.
149 M. Ide, A. Saeki, Y. Koizumi, T. Koganezawa and S. Seki, *J. Mater. Chem. A*, 2015, **3**, 21578–21585.
150 S.-C. Lan, C.-K. Chang, Y.-H. Lu, S.-W. Lin, A. K. Y. Jen and K.-H. Wei, *RSC Adv.*, 2015, **5**, 67718–67726.
151 I. Osaka, Y. Houchin, M. Yamashita, T. Kakara, N. Takemura, T. Koganezawa and K. Takimiya, *Macromolecules*, 2014, **47**, 3502–3510.
152 X. Zhang, L. J. Richter, D. M. DeLongchamp, R. J. Kline, M. R. Hammond, I. McCulloch, M. Heeney, R. S. Ashraf,

J. N. Smith, T. D. Anthopoulos, B. Schroeder, Y. H. Geerts, D. A. Fischer and M. F. Toney, *J. Am. Chem. Soc.*, 2011, **133**, 15073–15084.
153 H. G. Kim, B. Kang, H. Ko, J. Lee, J. Shin and K. Cho, *Chem. Mater.*, 2015, **27**, 829–838.
154 V. Vohra, K. Kawashima, T. Kakara, T. Koganezawa, I. Osaka, K. Takimiya and H. Murata, *Nat. Photonics*, 2015, **9**, 403–408.
155 J. Y. Na, B. Kang, D. H. Sin, K. Cho and Y. D. Park, *Sci. Rep.*, 2015, **5**, 13288.
156 Y.-W. Su, C.-M. Liu, J.-M. Jiang, C.-S. Tsao, H.-C. Cha, U. S. Jeng, H.-L. Chen and K.-H. Wei, *J. Phys. Chem. C*, 2015, **119**, 3408–3417.
157 J. J. van Franeker, M. Turbiez, W. Li, M. M. Wienk and R. A. Janssen, *Nat. Commun.*, 2015, **6**, 6229.
158 A. Sharenko, M. Kuik, M. F. Toney and T.-Q. Nguyen, *Adv. Funct. Mater.*, 2014, **24**, 3543–3550.
159 H. Yan, B. A. Collins, E. Gann, C. Wang, H. Ade and C. R. McNeill, *ACS Nano*, 2012, **6**, 677–688.
160 B. A. Collins, E. Gann, L. Guignard, X. He, C. R. McNeill and H. Ade, *J. Phys. Chem. Lett.*, 2010, **1**, 3160–3166.
161 B. A. Collins, J. E. Cochran, H. Yan, E. Gann, C. Hub, R. Fink, C. Wang, T. Schuettfort, C. R. McNeill, M. L. Chabinyc and H. Ade, *Nat. Mater.*, 2012, **11**, 536–543.
162 E. Gann, A. T. Young, B. A. Collins, H. Yan, J. Nasiatka, H. A. Padmore, H. Ade, A. Hexemer and C. Wang, *Rev. Sci. Instrum.*, 2012, **83**, 045110.
163 W. Ma, L. Ye, S. Zhang, J. Hou and H. Ade, *J. Mater. Chem. C*, 2013, **1**, 5023.
164 H. Yan, C. Wang, A. Garcia, S. Swaraj, Z. Gu, C. R. McNeill, T. Schuettfort, K. E. Sohn, E. J. Kramer, G. C. Bazan, T.-Q. Nguyen and H. Ade, *J. Appl. Phys.*, 2011, **110**, 102220.
165 W. Ma, J. R. Tumbleston, L. Ye, C. Wang, J. Hou and H. Ade, *Adv. Mater.*, 2014, **26**, 4234–4241.
166 B. A. Collins, Z. Li, J. R. Tumbleston, E. Gann, C. R. McNeill and H. Ade, *Adv. Energy Mater.*, 2013, **3**, 65–74.
167 L. Lu, W. Chen, T. Xu and L. Yu, *Nat. Commun.*, 2015, **6**, 7327.
168 L. Lu, T. Xu, W. Chen, E. S. Landry and L. Yu, *Nat. Photonics*, 2014, **8**, 716–722.
169 N. Zhou, X. Guo, R. P. Ortiz, T. Harschneck, E. F. Manley, S. J. Lou, P. E. Hartnett, X. Yu, N. E. Horwitz, P. M. Burrezo, T. J. Aldrich, J. T. Lopez Navarrete, M. R. Wasielewski, L. X. Chen, R. P. Chang, A. Facchetti and T. J. Marks, *J. Am. Chem. Soc.*, 2015, **137**, 12565–12579.
170 T. L. Nguyen, H. Choi, S. J. Ko, M. A. Uddin, B. Walker, S. Yum, J. E. Jeong, M. H. Yun, T. J. Shin, S. Hwang, J. Y. Kim and H. Y. Woo, *Energy Environ. Sci.*, 2014, **7**, 3040–3051.
171 M. Zhang, X. Guo, W. Ma, H. Ade and J. Hou, *Adv. Mater.*, 2015, **27**, 4655–4660.
172 L. Huo, T. Liu, B. Fan, Z. Zhao, X. Sun, D. Wei, M. Yu, Y. Liu and Y. Sun, *Adv. Mater.*, 2015, **27**, 6969–6975.
173 K. Sun, Z. Xiao, S. Lu, W. Zajaczkowski, W. Pisula, E. Hanssen, J. M. White, R. M. Williamson, J. Subbiah, J. Ouyang, A. B. Holmes, W. W. Wong and D. J. Jones, *Nat. Commun.*, 2015, **6**, 6013.
174 Q. Zhang, B. Kan, X. Wan, H. Zhang, F. Liu, M. Li, X. Yang, Y. Wang, W. Ni, T. P. Russell, Y. Shen and Y. Chen, *J. Mater. Chem. A*, 2015, **3**, 22274–22279.